Behaviour of apatite during partial melting of metapelites and consequences for prograde suprasolidus monazite growth

Chris Yakymchuk

Department of Earth and Environmental Sciences
University of Waterloo
Waterloo, Ontario, Canada, N2L 3G1
email: cyakymchuk@uwaterloo.ca

Abstract

The suprasolidus behaviour of apatite and monazite are examined for an average metapelite composition

using phase equilibria modelling coupled with solubility equations of these minerals. Both closed- and

open-system scenarios are considered. Partial melting above the solidus requires apatite and monazite

breakdown in order to saturate the anatectic melt in phosphorus and the light rare earth elements. In

general, melt loss is predicted to increase the stability of apatite and monazite at high temperature. Most

apatite is predicted to survive up to ultrahigh temperature conditions except for rocks with low bulk

phosphorus concentrations. By contrast, most monazite is expected to be consumed by UHT conditions.

Thorium substitution in monazite is expected to increase the stability of monazite to higher

temperatures. The presence of LREE-rich apatite decreases the stability of monazite above the solidus,

but the breakdown of this apatite during anatexis may generate prograde monazite at the apatite–melt

interface in local pockets of melt oversaturation. However, prograde suprasolidus monazite along grain

boundaries is expected to be consumed during further partial melting or during melt homogenization

when an interconnected melt network develops. Anatectic melts are predicted to be saturated with

respect to apatite except at UHT conditions and for rocks with low initial P_2O_5 bulk concentrations.

*Keywords***:** Accessory Minerals, Migmatite, Granulite, Partial Melting, Apatite, Monazite

1. Introduction

1

Apatite and monazite are ubiquitous minerals in aluminous metamorphic rocks and are the dominant repository for phosphorus and the light rare earth elements (LREE) in migmatites and granulites (e.g. Bea et al., 1994; Bea, 1996a, 1996b; Spear and Pyle, 2002; Prowatke and Klemme, 2006). While apatite is commonly used for geochronology of low-temperature processes (e.g. Farley and Stockli, 2002), monazite is frequently used to date portions of suprasolidus P–T paths in high-temperature metamorphic rocks (e.g. Parrish, 1990; Lederer et al., 2013; Taylor et al., 2016). Both minerals are expected to break down in suprasolidus metamorphic rocks during heating and anatexis in order saturate the anatectic melt in phosphorus and the LREE (e.g. Watson, 1979; Watson and Harrison, 1983; Rapp and Watson, 1986; Montel, 1986, 1993; Rapp et al., 1987; Pichavant et al., 1992; Wolf and London, 1994; London et al., 1999; Stepanov et al., 2012; Duc-Tin and Keppler, 2015).

Theoretical modelling of monazite behaviour in suprasolidus metamorphic rocks suggests that prograde monazite growth above the solidus is unlikely and that monazite ages record cooling and crystallization from anatectic melt (e.g. Kelsey et al., 2008; Spear and Pyle, 2010; Yakymchuk and Brown, 2014b). This contrasts with several studies that convincingly show that monazite can record prograde ages associated with heating and partial melting (e.g. Hermann and Rubatto, 2003; Dumond et al., 2015; Hacker et al., 2015; Johnson et al., 2015; Blereau et al., 2016). Therefore, the mechanisms that generate prograde monazite in suprasolidus metamorphic rocks are unclear. Furthermore, the behaviour of LREE-rich apatite during suprasolidus metamorphism has not yet been quantified using phase equilibria modelling, but the breakdown of this apatite and growth of monazite has been documented in experimental studies (e.g. Wolf and London, 1994) and has been proposed as a possible mechanism to produce prograde suprasolidus monazite (e.g. Johnson et al., 2015). However, the coupling of LREE-rich apatite to monazite behaviour during anatexis has yet to be evaluated using quantitative phase equilibria modelling because previous studies did not include phosphorus in their models (e.g. Kelsey et al., 2008; Yakymchuk and Brown, 2014b).

54   In this contribution, I first review the controlling factors for apatite and monazite dissolution in

55   anatectic melt. Then I combine phase equilibria modelling of an anatectic metapelite with the

56   experimental results of apatite and monazite dissolution to quantify the coupled behaviour of apatite and

57   monazite during anatexis as well as evaluate if the breakdown of LREE-rich apatite can trigger prograde

58   monazite growth above the solidus. Both closed-system and open-system (e.g. melt loss) scenarios are

59   considered. The consequences for phosphorus saturation of anatectic melts and granites with respect to

60   apatite are also discussed.

61

62   **2. Suprasolidus behaviour of apatite and monazite**

63   Apatite and monazite are the main carriers of phosphorus in suprasolidus metamorphic rocks and

64   their breakdown is required to maintain phosphorus saturation of melt during anatexis. In addition,

65   monazite is the primary repository of LREE in most metasedimentary rocks (Bea, 1996b) and it is the

66   main contributor of the LREE to anatectic melt. Monazite breakdown will also liberate phosphorus—an

67   essential structural constituent of monazite (~29 wt.% P_2O_5)—into the anatectic melt, although the

68   contribution is expected to be negligible compared with any phosphorus released from apatite

69   breakdown (e.g. London et al., 1999; García-Arias et al., 2012). Apatite can also contain significant

70   concentrations of the LREE (e.g. Bea et al., 1994) and its breakdown may release LREE into the melt.

71   Therefore, the breakdown and growth of apatite and monazite in suprasolidus systems depend on each

72   other; the breakdown of one may lead to oversaturation of the melt with respect to the other.

73   The breakdown of apatite and monazite into melt is controlled by chemical and physical factors,

74   including: temperature, pressure, melt chemistry and kinetics (Watson, 1979; Watson and Green, 1981;

75   Watson and Harrison, 1983; Rapp and Watson, 1986; Piccoli and Candela, 2002; Stepanov et al., 2012).

76   Several experimental studies have examined these factors for peraluminous melt compositions, which

77   are applicable to metapelites and metagreywackes (e.g. Harrison and Watson, 1984; Bea et al., 1992;

78   Pichavant et al., 1992; Wolf and London, 1994; Toplis and Dingwell, 1996; London et al., 1999).

79 Harrison and Watson (1984) used partial melting experiments to show that apatite solubility is

80 related to temperature and the SiO_2 concentration of melt by the following relationship:

81 $$lnD_P^{apatite/melt} = \left[\frac{(8400 + ((SiO_2 - 0.5)2.64 \times 10^4))}{T}\right] - [3.1 + 12.4(SiO_2 - 0.5))] \qquad (1)$$

82 where SiO_2 is the weight fraction in the melt and T is in Kelvin. This relationship is predicted to be valid

83 for melt with SiO_2 concentrations between 45% and 75%, for 0% to 10% wt.% H_2O and for the range of

84 pressures expected in the crust (Harrison and Watson, 1984). Pichavant et al. (1992) conducted

85 reconnaissance experiments and they demonstrated that apatite solubility increases for peraluminous

86 melt compositions compared with the metaluminous and peralkaline melts used by Harrison and Watson

87 (1984). Building on the work of these previous studies, Wolf and London (1994) derived a simple

88 equation that relates the aluminum saturation index (ASI: molar Al_2O_3 / [$Na_2O + K_2O + CaO$]) of the

89 melt to the concentration of P_2O_5 in melt that is in chemical equilibrium with apatite:

90 $$P_2O_{5\ (wt.\%)} = -3.4 + 3.1 \times ASI \qquad (2)$$

91 However, their experiments were restricted to low pressure (2 kbar) and peraluminous melt

92 compositions (ASI > 1,1), which may be applicable for partial melting of aluminous metasedimentary

93 rocks but not for intermediate to basic rocks.

94 The solubility of monazite in granitic melts has been investigated in several experimental studies

95 (Montel, 1986; Rapp and Watson, 1986; Rapp et al., 1987; Montel, 1993; Stepanov et al., 2012; Duc-Tin

96 and Keppler, 2015). Stepanov et al. (2012) combined their experimental results with previous work and

97 derived the following equation for monazite solubility:

98 $$ln\Sigma LREE = 16.16(\pm 0.3) + 0.23(\pm 0.07)\sqrt{H_2O} - \frac{11494(\pm 410)}{T} - 19.4(\pm 4)P/T + lnX_{mnz}^{LREE} \qquad (3)$$

99 where the amount of H_2O in melt is in wt.%, T is in Kelvin, P is in kbar, $\Sigma LREE$ is the sum of La–Sm

100 (in ppm) in the melt and X_{mnz}^{LREE} is the molar ratio of the LREE to the sum of all cations in monazite. In

101 general, monazite solubility is higher for increasing T and the H_2O concentration of the melt and

102 monazite solubility decreases with increasing pressure.

4

103

3. Methodology

3.1. Phase equilibria modelling

An average amphibolite-facies metapelite (Ague, 1991; Table 1) is used to model the

suprasolidus phase relations, melt compositions and behaviour of apatite and monazite during partial

melting. This composition is chosen because it is generally the most fertile rock type in metasedimentary

sequences and metapelites usually contain low-variance assemblages that are particularly useful for

metamorphic studies. Calculations were performed using THERMOCALC v.3.40 (Powell and Holland,

1988) and the internally consistent dataset of Holland and Powell (2011). Modelling was undertaken in

the $MnO–Na_2O–CaO–K_2O–FeO–MgO–Al_2O_3–SiO_2–H_2O–TiO_2–Fe_2O_3$ (MnNCKFMASHTO) chemical

system (e.g. White et al., 2014a, b). The activity–composition models are from White et al. (2014a).

Phases modelled as pure end-members include quartz, rutile, aqueous fluid (H_2O), kyanite and

sillimanite. Mineral abbreviations are from Holland and Powell (2011).

Suprasolidus rocks are generally not expected to have excess free H_2O due to the low

permeability of the deep crust and any free H_2O is likely partitioned into anatectic melt (White and

Powell, 2002; White et al., 2005). The solubility of H_2O in anatectic melt increases with pressure along

the wet solidus. For the phase equilibria modelling presented here, the amount of H_2O in the bulk

composition is adjusted so that the melt is just saturated with H_2O at solidus where the modelled

prograde path crosses the solidus. If the prograde path crossed the wet solidus at lower or higher

pressures, the quantity of melt produced will be slightly overestimated and underestimated, respectively.

Also, the melt at the wet solidus above this pressure will be slightly oversaturated in H_2O.

The average metapelite composition saturated with H_2O at the solidus at 9 kbar was used to

model closed-system behaviour. This does not account for melt loss, which is a path-dependent process

(e.g. Mayne et al., 2016; Guevara and Caddick, 2016) and this is discussed next. However, the closed-

127   system model is used as a baseline to assess the sensitivity of the modelling to different variables related

128   to the behaviour of apatite and monazite.

129

130   *3.2 Open-system behaviour*

131   The preservation of high-grade metamorphic assemblages in migmatites and granulites requires

132   the loss of anatectic melt (e.g. Spear et al., 1999; White and Powell, 2002). Melt loss during anatexis has

133   important implications for the behaviour of major and accessory minerals during metamorphism (e.g.

134   Yakymchuk and Brown, 2014b) as well as the concentration of the LREE and phosphorus in the

135   residuum (e.g. Rapp et al., 1987). The effects of melt loss on the behaviour of apatite and monazite are

136   modelled for two schematic *P–T* paths that involve isobaric heating from the solidus up to 950°C at 9

137   kbar and 6 kbar. The higher pressure isobaric path was chosen to approximate a typical prograde path

138   for collisional orogenesis (e.g. Clark et al., 2011) and the lower pressure path to model the reaction

139   sequence experienced by high-pressure–low-temperature terranes (e.g. Kelsey and Hand, 2015). For the

140   isobaric heating path at 6 kbar, the starting bulk composition is adjusted so that the melt is just saturated

141   with H_2O at solidus at this pressure.

142   Melt loss is modelled following the methodology of Yakymchuk and Brown (2014a, b) whereby

143   6 mol.% of melt is extracted out of the system when the total amount reaches 7 mol.% (approximately

144   equivalent to 7 vol.% on a one-oxide basis). The modelled 7 vol.% threshold approximates the melt

145   connectivity threshold of Rosenberg and Handy (2005). The extraction of 6 mol.% melt leaves 1 mol.%

146   melt in the system. The extracted melt has a major element composition determined from the phase

147   equilibria modelling and phosphorus and LREE concentrations determined from the saturation models

148   above (equations 1–3) as long as apatite and monazite are present in the system to buffer the

149   concentrations. After each melt loss event, the melt-depleted composition is used to model the next

150   segment of the isobaric heating path up to the next melt loss event. This process is repeated until the end

151   of each isobaric heating path is reached at 950°C.

152

153   *3.3. Monazite and apatite behaviour*

154   The amounts of apatite and monazite dissolution and growth are modelled by similar methods to

155   those reported in Kelsey et al. (2008). The limitations and assumptions of this approach are discussed

156   later. First, the saturation concentrations of the melt in ppm are calculated as follows. The major element

157   concentration of the anatectic melt at *P–T* is calculated using THERMOCALC every 1°C and 0.1 kbar

158   across the suprasolidus portion of the pseudosection shown in Figure 1. This information is combined

159   with experimentally determined solubility equations for apatite of Harrison and Watson (1984; HW84)

160   as well as Wolf and London (1994; WL94). Both equations are used because they are both applicable to

161   peraluminous melts, but they yield different results. The solubility equation for monazite is from

162   Stepanov et al. (2012). The solubility equations are combined with assumed stoichiometric

163   concentrations of phosphorus in apatite (41 wt.% P_2O_5; the average of apatite compositions reported in

164   Webster and Piccoli, 2015), LREE in monazite (566,794 ppm; Kelsey et al., 2008) and phosphorus in

165   monazite (29 wt.% P_2O_5). The result is the saturation concentration of phosphorus (P_{Sat}) and the LREE

166   ($LREE_{Sat}$) in the anatectic melt at each *P–T* point. These 'initial saturation concentrations' are

167   independent of the proportion of anatectic melt and the bulk concentrations of phosphorus and LREE.

168   Three bulk rock values of P_2O_5 (0.1, 0.3 and 0.5 wt.%) are used that represent the typical range

169   of measured compositions in pelites (e.g. Ague, 1991; London et al., 1999). A bulk LREE concentration

170   of 150 ppm is used that is representative of pelites and metasedimentary migmatites (e.g. Taylor and

171   McLennan, 1985; Yakymchuk and Brown, 2014b).

172   At this point the methodology departs from that of Kelsey et al. (2008) in order to couple the

173   behaviour of monazite to that of apatite. All of the phosphorus and LREE in the bulk rock are assumed

174   to reside only in apatite, monazite and melt. No phosphorus substitution into major minerals is

175   considered; the possible effects of this are discussed later. The amounts of these elements are then

176   allocated from the bulk concentrations of phosphorus and LREE to form apatite and monazite based on

7

177 three values: (1) the bulk concentration of LREE in ppm ($LREE_{Bulk}$), (2) the bulk concentration of

178 phosphorus in ppm (P_{Bulk}), and (3) the concentration of LREE in apatite in ppm (Ap_{LREE}). The

179 concentration of LREE in apatite will vary with melt composition (Prowatke and Klemme, 2006) due to

180 partitioning of LREE between apatite and melt and the concentration of LREE in apatite can be

181 determined by:

182
$$Ap_{LREE} = D_{LREE}^{Ap/melt} \times LREE_{melt} \quad (4)$$

183 where $D_{LREE}^{Ap/melt}$ is the partition coefficient of LREE between apatite and melt and $LREE_{melt}$ is equal to

184 $LREE_{Sat}$ when monazite is present in the system. Here, I use a $D_{Ap/melt}^{LREE}$ value of 10, which is an average

185 of the experimental results reported in Prowatke and Klemme (2006) for La partitioning between apatite

186 and melt for melts with concentrations of >45 wt.% SiO_2. The amounts of phosphorus in apatite (Ap_P)

187 and monazite (Mnz_P) and LREE in monazite (Mnz_{LREE}) are fixed to the stoichiometric values stated

188 above.

189 The bulk concentration of phosphorus and LREE is the sum of these elements allocated to each

190 mineral:

191
$$P_{Bulk} = P_{Ap} + P_{Mnz} \quad (5)$$

192
$$LREE_{Bulk} = LREE_{Ap} + LREE_{Mnz} \quad (6)$$

193 where P_{Ap} and P_{Mnz} are the amounts of phosphorus allocated to form apatite and monazite, respectively

194 and $LREE_{Ap}$ and $LREE_{Mnz}$ are the amount of LREE allocated to form apatite and monazite, respectively.

195 Starting with the assumption that all LREE in the rock resides in monazite ($LREE_{Bulk} =$

196 $LREE_{Mnz}$), and that the ratio of $\frac{Mnz_P}{Mnz_{LREE}}$ is fixed, the amount of phosphorus needed to form stoichiometric

197 monazite is calculated as follows:

198
$$P_{mnz} = \frac{Mnz_P}{Mnz_{LREE}} \times LREE_{Mnz} \quad (7)$$

199 The remaining amount of phosphorus that is allocated to form apatite is then calculated by rearranging

200 equation (5):

201
$$P_{Ap} = P_{bulk} - P_{mnz} \quad (8)$$

202 Using this amount of phosphorus available to form apatite, the amount of LREE allocated to make

203 apatite with the concentration of LREE *(Ap_LREE)* determined by partitioning between apatite and melt

204 (equation 4) is then calculated:

205
$$LREE_{Ap} = \frac{P_{Ap}}{\frac{Ap_P}{Ap_{LREE}}} \quad (9)$$

206 The amount of LREE remaining to form monazite is then calculated by rearranging equation (6):

207
$$LREE_{Mnz} = LREE_{Bulk} - LREE_{Ap} \quad (10)$$

208 Here, the revised amount of LREE allocated to monazite ($LREE_{Mnz}$) is inserted back into equation (7)

209 and this series of equations (7–10) is solved iteratively to determine the amounts of phosphorus and

210 LREE allocated to apatite and monazite, respectively. These values are equivalent to the 'effective'

211 concentrations of Kelsey et al. (2008) and Yakymchuk and Brown (2014b) and are independent of the

212 amount of melt in the system.

213   The saturation concentrations of phosphorus (P_{Sat}) and the LREE ($LREE_{Sat}$) calculated from the

214 solubility equations of apatite and monazite (Harrison and Watson, 1984; Wolf and London, 1994;

215 Stepanov, al. 2012) are now divided by the allocated values of phosphorus to apatite (P_{Ap}) and the

216 LREE to monazite ($LREE_{Mnz}$) and multiplied by the fraction of anatectic melt at *P–T* retrieved from

217 THERMOCALC to arrive at the fraction of apatite and monazite dissolution (*Ap_diss* and *Mnz_diss*) required to

218 saturate the anatectic melt in these elements (e.g. Kelsey et al., 2008):

219
$$Ap_{diss} = \frac{P_{Sat}}{P_{Ap}} \times melt\ fraction \quad (11)$$

220
$$Mnz_{diss} = \frac{LREE_{Sat}}{LREE_{Mnz}} \times melt\ fraction \quad (12)$$

221   Finally, this last calculation is repeated considering the amount of LREE contributed by the

222 breakdown of apatite and the amount of phosphorus contributed by the breakdown of monazite:

223
$$Ap^{*}_{diss\%} = \left[\frac{P_{Sat}}{P_{Ap} + (Mnz_{diss} \times P_{Mnz})}\right] \times melt\ fraction \times 100 \quad (13)$$

224
$$Mnz^*_{diss\%} = \left[\frac{LREE_{Sat}}{LREE_{Mnz} + (Ap_{diss} \times LREE_{Ap})} \right] \times melt\ fraction \times 100 \qquad (14)$$

225   The result is the percentage of apatite ($Ap^*_{diss\%}$) and monazite ($Mnz^*_{diss\%}$) dissolution required to

226   saturate the volume of anatectic melt in phosphorus and the LREE with respect to apatite and monazite.

227   These values are plotted on a *P–T* grid and are contoured for closed-system scenarios.

228   For the open-system scenarios, the same equations are employed except that the effective bulk

229   composition of phosphorus (P_{bulk}) and the LREE ($LREE_{Bulk}$) change along the *P–T* path after melt loss

230   events. Similar to the closed system scenario, three initial bulk compositions of P_2O_5 are investigated

231   (0.1, 0.3 and 0.5 wt.%) for open-system behaviour and the initial bulk composition of LREE is set at 150

232   ppm.

233   The equations above are used when the system contains apatite and monazite to buffer the

234   concentration of phosphorus and the LREE in melt (P_{Sat} and $LREE_{Sat}$, respectively). In scenarios where

235   monazite is completely consumed, the LREE concentrations of melt and apatite are determined by the

236   partitioning expression in equation (4). In scenarios where monazite and apatite are both completely

237   consumed, the concentrations of phosphorus and the LREE in melt are calculated from the proportion of

238   melt in the system and the effective bulk compositions of phosphorus (P_{bulk}) and LREE ($LREE_{Bulk}$).

239

240   **4. Results for a closed system**

241   *4.1 Phase relations*

242   The *P–T* pseudosection for the amphibolite-facies metapelite is shown in Figure 1. The mineral

243   assemblages are typical of those found in metasedimentary migmatites at the amphibolite and granulite

244   facies. Ilmenite and plagioclase are stable in each suprasolidus field across the modelled *P–T* range.

245   Rutile is restricted to high pressures ($P > 10$–11.5 kbar). The important peritectic minerals in the

246   modelled composition are K-feldspar, garnet, and cordierite. K-feldspar is stable at *T*> 660–770°C with

247   increasing pressure. Garnet is stable across the diagram except at *T* < 700°C at *P* < 5.5 kbar. Cordierite

10

248   is stable at $P < 4$–7 kbar with increasing temperature. Orthopyroxene is not stable in the modelled P–T

249   range.

250   The four important partial melting reactions for the metapelite include, from low T to high T: (1)

251   the consumption of a minimal amount of free H_2O to produce melt at the wet solidus, (2) the breakdown

252   of muscovite to produce peritectic K-feldspar, which is represented by a narrow low-variance field that

253   extends from the wet solidus at ~4 kbar up to 780°C at 12 kbar, (3) the progressive consumption of

254   biotite to produce peritectic garnet at higher pressure or peritectic cordierite at lower pressure, and (4)

255   the consumption of quartz and feldspar to produce progressively drier melt at temperatures above biotite

256   exhaustion (>900°C). Quartz is predicted to be completely consumed at 820–950°C with increasing

257   pressure. These melting reactions are similar to those documented in experimental melting studies

258   (Clemens, 2006) and in migmatites terranes (e.g. Brown, 2013) for metasedimentary rocks.

259

260   *4.2 Melt proportions and composition*

261   The proportion of melt predicted at P–T in the metapelite is shown in Figure 2a for a closed

262   system. Melt isopleths are positively sloping to nearly vertical. Therefore, melting can proceed through

263   heating or decompression in a closed-system scenario. However, this may not be the case for open-

264   system scenarios (e.g. Yakymchuk and Brown, 2014a). Note that the melt contours are not evenly

265   spaced, which indicates that melt production is non-linear with heating.

266   The composition of the melt varies across the pseudosection and the important compositional

267   parameters for apatite and monazite dissolution are shown in Figure 2b–d. Melt ASI increases as

268   temperature increases (Fig. 2b), which reflects the progressive breakdown of muscovite and biotite.

269   Contours for ASI are positively sloping on the pseudosection in the stability field of an aluminosilicate

270   mineral (sillimanite and kyanite) and are negatively sloping below the sillimanite-out line in the low P

271   and high T portion of the pseudosection. This indicates that the solubility of apatite is expected to

272   increase during prograde metamorphism and anatexis for the WL94 model of apatite solubility.

273   The weight fraction of SiO_2 in the anatectic melt generally increases up temperature, with the

274   exception of low P and high T where it decreases up temperature due to the exhaustion of quartz (Fig.

275   2c). Contours for the weight fraction of SiO_2 have moderate positive slopes at low T and shallower

276   slopes at low P and high T (Fig. 2c). An increase in SiO_2 is expected to decrease the solubility of apatite

277   in melt and an increase in temperature increases the solubility of apatite (e.g. Harrison and Watson,

278   1984).

279   Contours of the weight fraction of H_2O in melt have positive slopes across the diagram and the

280   values decrease up temperature (Fig. 2d). The decrease of the H_2O content of melt during heating

281   reflects the increasing contribution of anhydrous reactants in melt-producing reactions during heating.

282   For example, after biotite is exhausted, melting proceeds mostly through the breakdown of quartz and

283   feldspar. Based on the solubility equation of Stepanov et al. (2012), monazite solubility is expected to

284   decrease in drier melt. However, this decrease in solubility may be counteracted during prograde

285   metamorphism by the increase in temperature (e.g. Yakymchuk and Brown, 2014b).

286

287   *4.3 Phosphorus and LREE saturation of the melt*

288   The saturation values of phosphorus (P_{Sat}) and the LREE ($LREE_{Sat}$) for the metapelite over the

289   modelled P–T range are shown in Figure 3. For apatite, the HW84 solubility equation predicts P_2O_5

290   concentrations of up to 0.18 wt.% at 950°C and the saturation concentrations are mostly temperature

291   dependent (Fig. 3a). By contrast, the WL94 model predicts substantially higher concentrations of up to

292   ~0.60 wt.% P_2O_5 at 950°C and they are strongly correlated with melt ASI (Figs 2b, 3b). Note that the

293   WL94 model does not work for ASI values <1.1 (Fig. 2b). Therefore, this model is not applicable for the

294   high P and low T portion of the diagram (Fig. 3b). LREE saturation contours are nearly vertical, which

295   indicates that they are mostly sensitive to temperature (Fig. 3c). Monazite solubility is also sensitive to

296   the concentration of H_2O in melt, which decreases during heating for the modelled composition (Fig.

297   2d).

298

4.4 Apatite behaviour

The two different apatite solubility equations (HW84 vs. WL94; equations 1 and 2) yield

different results for the behaviour of apatite. For the HW84 solubility equation, apatite dissolution

contours are positively sloping and nearly vertical (Fig. 4b, d, f); this is similar to the slope of melt

contours in Fig. 2a. The amount of apatite dissolution is non-linear and the spacing of contours

decreases at progressively higher temperatures. At 9 kbar and 900°C, the predicted amounts of apatite

dissolution for the three modelled bulk compositions vary from to 45% for low P_2O_5 concentrations

(0.10 wt.%), 18% for intermediate concentrations (0.30 wt.% P_2O_5), and 10% at higher concentrations

(0.50 wt.% P_2O_5). Complete apatite dissolution is predicted only for the low P_2O_5 concentration at

T>930°C at P<9 kbar (Fig. 4f).

For the WL94 model, the dissolution contours are strongly correlated with melt ASI (Fig. 2b)

and are positively sloping at low T as well as at high P and negatively sloping at P< 5 kbar at high T

(Fig. 4a, c, e). The transition from positive to negative slope generally coincides with the sillimanite-out

field boundary (Fig. 1). When compared with the results with the HW84 solubility equation, the WL94

model predicts more apatite dissolution across the investigated P–T range (Fig. 4). For both apatite

dissolution models, apatite is predicted to grow during cooling and melt crystallization. The breakdown

of monazite contributes minimal phosphorus to the melt (e.g. London et al., 1999; Garcia-Arias et al.,

2012) and the dissolution of apatite is essentially independent of any phosphorus released from monazite

breakdown.

318

4.5 Monazite behaviour

The predicted stability of monazite at suprasolidus conditions is shown in Fig. 5 for three closed-

system scenarios. For the first scenario, LREE liberated from apatite breakdown is not considered (e.g.

Kelsey et al., 2008; Yakymchuk and Brown, 2014b). For the second scenario, apatite breakdown is

13

323   modelled using the HW84 solubility equation and LREE is partitioned between apatite and melt using

324   equation 4. The third scenario is similar to the second except that the WL94 solubility equation for

325   apatite is used.

326   All three scenarios yield positively sloping contours for monazite dissolution that are kinked in

327   the narrow low-variance muscovite–K-feldspar and sillimanite–cordierite fields (Figs 1, 5); this reflects

328   the large quantity of melt produced in these relatively narrow fields, which requires a large proportion of

329   monazite dissolution to maintain melt saturation in the LREE. The main difference between the

330   monazite-only model (scenario 1) and the models that include LREE partitioning between apatite and

331   melt (scenarios 2 and 3) is that the dissolution contours for monazite are shifted down temperature by

332   ~10–20°C (Fig. 5b, c). This reflects the reduced effective bulk composition of LREE in the system

333   available to monazite due to the sequestration of some LREE into apatite.

334

335   **5. Results for an open system**

336   The reaction sequence for the modelled isobaric heating paths at 9 kbar and 6 kbar are compared for

337   closed and open-system scenarios in Figure 6a–d. For the 9 kbar heating path, five melt loss events

338   occur during heating resulting in the extraction of 30 mol.% melt from the system. The quantity of melt

339   produced in the open-system scenario (32 mol.%) is roughly half of the amount generated in a closed

340   system (60 mol.%). For the 6 kbar heating path, six melt loss events are predicted to occur during

341   heating and the quantity of melt produced in the open-system scenario (39 mol.%) is also roughly half of

342   the amount generated in a closed system (66 mol.%). While there are subtle differences in the reaction

343   sequence and stability of minerals between closed- and open-system scenarios (e.g. the stability of

344   quartz to higher T in open-system scenarios), the principle effect of progressive melt loss is the reduced

345   fertility of the residuum. The differences of important melt composition variables for apatite and

346   monazite solubility in melt (ASI, SiO_2, H_2O) are negligible (<2% difference) between the closed- and

347 open-system models at the same P–T condition. Therefore, Figures 2b–d and 3 are broadly applicable

348 for evaluating both closed- and open-system behaviour during isobaric heating.

349   For the open-system scenarios, bulk rock values of P_2O_5 and LREE change along the P–T path at

350 each melt loss event for both modelled P–T paths (Fig. 6e–l). Changes in the concentrations of P_2O_5 and

351 LREE in the melt phase are shown in Figure 7 for calculations using the WL94 apatite solubility

352 equation. If concentrations of P_2O_5 and LREE in melt (Fig. 7)—which are equivalent to the saturation

353 concentrations of phosphorus (P_{Sat}) and the LREE ($LREE_{Sat}$) if apatite and monazite are present—are

354 higher than the effective compositions (P_{bulk} and $LREE_{Bulk}$), then the residue will become depleted in

355 these elements after melt extraction (Fig. 6e–l). Extraction of melt with lower concentrations of

356 phosphorus and the LREE will result in elevated residuum concentrations of these elements. For

357 example, the P_2O_5 value of the residue increases after melt loss events for the isobaric heating path at 9

358 kbar and the starting compositions of 0.3 and 0.5 wt.% P_2O_5 (Fig. 6e, f) because the melt contains lower

359 concentrations of these elements (Fig. 7a). By contrast, there is a step-wise decrease in the P_2O_5 value of

360 the residuum for the isobaric heating path at 6 kbar and starting P_2O_5 concentration of 0.1 wt.% using

361 the WL94 solubility equation (Fig. 6g) because the P_2O_5 concentration of the extracted melt is >0.1

362 wt.% (Fig. 7c). The concentration of LREE in melt (Fig. 7b, d) is higher than the bulk composition at

363 each melt loss event and the residue becomes more depleted in LREE after each melt loss event (Fig. 6i–

364 l).

365   The amounts of apatite and monazite dissolution along the isobaric heating paths are compared

366 for closed- and open-system scenarios in Figure 8. The modes of apatite and monazite decrease during

367 heating for both scenarios. Melt loss increases the stability of apatite and monazite to higher

368 temperatures in open systems relative to the closed-system scenarios.

369   The stability of apatite to higher temperatures for the open-system scenarios reflects both the

370 progressive enrichment of the residue in P_2O_5 in most cases (Fig. 6e–g) and the reduced fertility of the

371 metapelite during progressive melt extraction along the isobaric heating path (Fig. 6a–d). An extreme

372   case is for a starting P_2O_5 value of 0.1 wt.% using the WL94 solubility equation for the isobaric heating

373   path at 9 kbar. For the closed system, apatite is expected to be completely consumed at ~880°C (Fig.

374   8a). For the open system, less than 30% of the amount of apatite present at the solidus is predicted to be

375   consumed by 950°C (Fig. 8a).

376   The increased stability of monazite to higher temperatures mainly reflects the reduced fertility of

377   the metapelite. The decrease in the LREE value of the residue during melt loss only has a subordinate

378   effect. The difference between closed- and open-system scenarios for monazite stability are apparent at

379   higher temperatures where there is significant divergence between the dissolution curves for the

380   different scenarios (Fig. 8e–h). Again, this reflects the reduced fertility of the metapelite after several

381   melt-loss events (Fig. 6a–d).

382

383   **6. Discussion**

384   *6.1. Limitations of modelling*

385   The limitations of the modelling approach applied here for monazite behaviour are detailed in

386   Kelsey et al. (2008), Yakymchuk and Brown (2014), and are also discussed by Taylor et al. (2016).

387   There are some additional limitations that apply to modelling apatite behaviour in this study. No

388   adjustment was made to the average metapelite composition to account for Ca in apatite in the phase

389   equilibria modelling. The modelling does not consider fluorine and chlorine, which can be important for

390   apatite stability in some magmatic, hydrothermal and metamorphic systems (e.g. Bingen et al. 1996;

391   Piccoli and Candela, 2002; Webster and Piccoli, 2015). Model apatite is assumed to have homogeneous

392   zoning in trace elements, although natural apatite can be zoned (e.g. Rakovan and Reeder, 1996; Smith

393   and Yardley, 1999; Yang and Rivers, 2002).

394   Apatite and monazite are modelled here as stoichiometric minerals (Apatite: $Ca_5(PO_4)_3(OH)$, and

395   monazite [LREE]PO_4). Consequently, the value of X_{mnz}^{LREE} in the Stepanov et al. (2012) monazite

396   solubility equation (equation 3 above) is 1. This approach ignores potentially important components

397   such as Th, U and Pb. Thorium concentrations in monazite usually range between 1–10 wt.% (e.g.

398   Stepanov et al., 2012), but can be up to 30 wt.% of some monazite (e.g. Catlos, 2013). A consequence of

399   considering Th substitution in monazite for the modelling presented here is that LREE saturation value

400   of equation (3) will decrease. Consequently, less LREE will be allocated to apatite in the bulk

401   composition ($LREE_{Ap}$), which is controlled by the LREE concentration of the melt (equation 4). The net

402   effect is that high-Th monazite is expected to persist to higher temperatures than Th-poor monazite.

403   Various values of X_{mnz}^{LREE} assuming Th substitution in monazite are investigated along the open-

404   system isobaric heating paths using the WL94 apatite solubility equation in Fig. 9. Note that the

405   calculations for monazite dissolution require an adjustment of the LREE composition of monazite

406   (Mnz_{LREE}) to account for Th substitution. For the 6 kbar isobaric heating path, the stability of monazite is

407   increased by ~50°C at high temperature for an X_{mnz}^{LREE} value of 0.7 (Fig. 9b). The high-temperature limit

408   of monazite stability is more significant for the 9 kbar heating path where ~30% of the monazite

409   originally present at the solidus is preserved at 950°C for an X_{mnz}^{LREE} value of 0.7 (Fig. 9a).

410   Although apatite and monazite are the main mineral repositories of phosphorus in most suprasolidus

411   metamorphic rocks, garnet and plagioclase can accommodate significant quantities of phosphorus (e.g.

412   Pyle and Spear, 2002; Villaseca et al., 2003; Kohn and Malloy, 2004; Dumond et al., 2015). For

413   example, ultrahigh-temperature granulites from Connecticut contain garnet with P_2O_5 concentrations up

414   to 0.4 wt.% (Ague and Eckert, 2012; Axler and Ague, 2015a, b). In the modelling here, the result of

415   garnet accommodating phosphorus is a reduction of phosphorus in the system allocated to apatite and an

416   increase in the amount of apatite dissolution required to maintain phosphorus saturation of melt. For the

417   modelled prograde heating paths and for both closed- and open-system scenarios (Fig. 6a–d), the

418   increasing mode of garnet would result in the partitioning of a greater proportion of the bulk phosphorus

419   into garnet as temperature increased. This would decrease the amount of phosphorus allocated to apatite

420   and may accelerate the consumption of apatite. However, the same heating paths would also consume

421   plagioclase, which may release some phosphorus into the system and contribute to phosphorus

422   saturation of the melt.

423   The consequences of garnet and plagioclase behaviour on the modes of apatite (and monazite) may

424   need to be considered in some cases where these major minerals are important hosts for phosphorus.

425   However, these minerals are generally expected to only contain a few percent of the total phosphorus

426   budget for metamorphic rocks. For example, a simple mass balance calculation by Spear and Pyle

427   (2002) estimate that a rock with 10 modal % garnet with 200 ppm phosphorus accounts for ~6% of the

428   phosphorus budget of the entire rock. Furthermore, the covariation between LREE and phosphorus

429   concentrations in some migmatites and anatectic granites suggests that the accessory minerals are the

430   main control on these elements during anatexis (e.g. Watt and Harley, 1993; Zeng et al., 2005a; Brown

431   et al., 2016).

432

433   *6.2 Kinetic controls on apatite and monazite dissolution*

434   The modelling presented here assumes equilibration of the anatectic melt in major and trace

435   elements. However, kinetics may inhibit apatite and monazite dissolution during partial melting, which

436   may lead to undersaturation of the melt in phosphorus and the LREE (e.g. Bea et al., 1994; Ayers and

437   Harris, 1997; Zeng et al., 2005a). The kinetics of apatite and monazite dissolution into anatectic melt are

438   sensitive to grain size, temperature and the H_2O content of the melt (e.g. Rapp and Watson, 1986;

439   Harrison and Watson, 1984). For a melt with 6 wt.% H_2O, it is predicted to take a maximum of ~1 ky at

440   750°C and <100 years at 950°C to dissolve a 500μm diameter apatite crystal (Fig. 10a; Harrison and

441   Watson, 1984). For a dry melt, a 500μm diameter apatite crystal is expected to take >10 My to

442   completely dissolve at 950°C (Fig. 10a). However, a completely dry melt composition is unrealistic for

443   the modelled metapelite composition for both closed- and open-system scenarios; the lowest modelled

444   H_2O content of melt in both scenarios is ~2 wt.% H_2O.

18

445   For monazite, Rapp and Watson (1986) evaluated the maximum time it takes to completely

446   consume monazite grains of various sizes. It is expected to take ~1 My at 750°C and <100 years at

447   950°C to completely dissolve a 50μm grain of monazite in a melt with 6 wt.% H_2O (Fig. 10b). For a

448   drier melt with 1 wt.% H_2O, the same monazite grain is predicted to take >1 Gy at 750°C and ~1 My at

449   950°C to completely dissolve (Fig. 10b).

450   For the modelled metapelite composition, the H_2O content of the melt decreases up temperature

451   for closed-system and open-system scenarios. The difference in the predicted H_2O content of melt

452   between these different scenarios is negligible (<0.2 wt.%) at the same $P–T$ condition. Although drier

453   melt compositions are expected to hinder monazite dissolution, this is counteracted by the increase in

454   temperature. For example, the H_2O content of melt at 9 kbar and 750°C is 9.5 wt.% (Fig. 2d). At these

455    $P–T$ conditions a 50μm grain of monazite is predicted to take <1 My to completely dissolve (Fig. 10b).

456   A similar duration is expected for a melt with ~3 wt.% H_2O at 9 kbar and 950°C (Fig. 10b).

457   The timescales of most regional high-temperature metamorphic processes range from millions to

458   tens of millions of years (e.g. Hermann and Rubatto, 2003; Clark et al., 2011; Harley, 2016). In general,

459   the timescales for apatite and monazite dissolution for the modelled average metapelite are expected to

460   be <1 My for anatectic melt with realistic H_2O concentrations (>1 wt.%). Therefore, kinetics are not

461   expected to hinder apatite and monazite dissolution in long-lived migmatite terranes except possibly for

462   large grains of apatite (> 500 μm) and monazite (> 50 μm) or if non-equilibrated melt is periodically

463   extracted at <1 My intervals (e.g. Sawyer, 1991; Ayers and Harris, 1997).

464

465   *6.3 Prograde monazite growth in migmatites*

466   Theoretical modelling of monazite behaviour in suprasolidus metamorphic rocks predicts that

467   prograde monazite growth above the solidus is unlikely because monazite breakdown is required for

468   LREE-saturation of the increasing amount of anatectic melt generated during heating (e.g. Kelsey et al.,

469   2008; Spear and Pyle, 2010; Yakymchuk and Brown, 2014b). Similarly, the modelling here suggests

470   that apatite will be consumed during heating and partial melting and grow as melt crystallizes during

471   cooling to the solidus for both closed- and open-system scenarios. Because apatite is generally stable to

472   higher temperatures than monazite (Fig. 8) and partitions some of the LREE in the system, the result is a

473   reduced stability of monazite when compared with an apatite-free model of monazite dissolution.

474   Therefore, no new monazite is predicted to grow during heating and partial melting including from the

475   breakdown of LREE-rich apatite in an equilibrated system.

476   If monazite is exhausted during prograde metamorphism, the concentration of LREE in the melt

477   will be governed by the partitioning of LREE between it and apatite and the LREE concentration of the

478   melt will decrease with further partial melting due to dilution (e.g. Klimm et al., 2008). The melt will

479   remain undersaturated with respect to monazite for the remainder of the prograde path and no new

480   monazite growth is expected.

481   Johnson et al. (2015) suggested that the breakdown of LREE-rich apatite during prograde

482   metamorphism may have liberated enough LREE to oversaturate the melt and grow monazite due to an

483   increase in melt ASI during progressive partial melting. However, the results of the modelling here

484   suggest that the increase in ASI appears to be counteracted by the non-linear increase in the generation

485   of melt during heating in a closed system (Fig. 6a, c), which requires progressively more apatite (and

486   monazite) dissolution to achieve phosphorus saturation of the melt. For an open system, the fertility of

487   the system decreases after melt loss (Fig. 6b, d), but monazite is still expected to be consumed during

488   heating to saturate the melt in LREE and no new growth is expected (Fig. 8e–h). Both of the modelled

489   scenarios assume that the melt is homogeneous and saturated in phosphorus (with respect to apatite)

490   during the entire metamorphic evolution except at *P–T* conditions above apatite exhaustion.

491   One of the key assumptions of a homogeneous melt composition in this study may not be valid if

492   there is sluggish diffusion of phosphorus and/or LREE away from apatite during dissolution. Wolf and

493   London (1995) suggested that monazite can grow along the apatite–melt interface due to local

494   oversaturation of LREE during apatite breakdown. This is because the diffusivities of REE and

495   phosphorus are generally similar (e.g. Rapp and Watson, 1986) whereas the diffusivity of calcium is

496   approximately two orders of magnitude higher (Harrison and Watson, 1984). Consequently, a narrow

497   region of melt adjacent to apatite may become enriched in LREE and phosphorus relative to the

498   surrounding melt and may be locally saturated with respect to monazite. This has been called 'pileup'

499   where diffusion away from the crystal interface is too slow to keep up with melt equilibration (e.g.

500   Green and Watson, 1982; Harrison and Watson, 1984). Therefore, although monazite crystallization

501   from apatite breakdown is not predicted by the phase equilibria modelling in this study for both closed-

502   and open-system scenarios, new monazite growth may occur in systems where the melt composition is

503   not homogeneous.

504   The extent of melting may have important implications for melt homogenization. Partial melting

505   begins at reactant grain junctions (e.g. Sawyer, 1999; Acosta-Vigil et al., 2006) in migmatites and melt

506   initially accumulates in isolated pockets. Further heating will increase the proportion of melt in the

507   system and the migmatite will eventually develop an interconnected melt network that physically links

508   individual melt pockets (e.g. Holness et al., 2011; Sawyer, 2014). This may lead to melt extraction from

509   the system as modelled above for the open-system scenarios. Isolated melt pockets have the potential to

510   become oversaturated with respect to monazite if LREE-rich apatite is in contact with the melt and

511   diffusion is sluggish. However, once an interconnected melt network develops, this will drive the system

512   towards homogenization and the preservation of oversaturated melt with respect to monazite (and

513   apatite) becomes less likely. Rosenberg and Handy (2005) estimated that melt interconnectivity may

514   occur when the melt proportion reaches ~7 vol.% in a static system. This value may be much less in a

515   dynamic system undergoing syn-anatectic deformation (Vigneresse and Burg, 2000; Brown, 2013),

516   which is more applicable to regional migmatite terranes that are generally very weak during anatexis

517   (e.g. Diener et al., 2014). For a closed system, the preservation of prograde monazite from the

518   breakdown of apatite is more likely in migmatites that have not undergone extensive partial melting or

519   where melt does not form an interconnected network. For open-system scenarios, isolated melt pockets

520   may become temporarily connected, but in general they evolve independent from each other and have a

521   greater likelihood of reaching local LREE oversaturation with respect to monazite.

522   Monazite growth at the margin of consumed apatite has been documented in experiments (Wolf

523   and London, 1995; García-Arias et al., 2012) and in studies of metamorphic rocks (e.g. Harlov et al.,

524   2007; Finger and Krenn, 2007; Rocha et al., 2016). Wolf and London (1995) described small (~30 µm)

525   monazite grains at the apatite–melt interface in their experiments. Similarly, Harlov et al. (2007)

526   documented small (<20 µm) monazite crystals at the margin of apatite in granulites from the Variscan

527   Schwarzwald of southern Germany. García-Arias et al. (2012) found <10 µm monazite grains around

528   apatite generated during experimental melting of an Iberian orthogneiss. Considering the kinetic

529   modelling of previous studies (Fig. 10; Harrison and Watson, 1984; Wolf and London, 1995), the

530   predicted dissolution times for these grain sizes are <1 My except for unrealistically dry melt

531   compositions. Therefore, prograde monazite produced through apatite breakdown is expected to be

532   consumed during melt equilibration and/or further partial melting. However, if these crystals are

533   included into a growing peritectic mineral (e.g. garnet), then they have a higher preservation potential.

534   As suggested by Wolf and London (1995), small monazite inclusions encased in minerals may reflect

535   earlier (e.g. prograde) growth whereas larger monazite grains in the matrix may grow from crystallizing

536   residual anatectic melt during cooling.

537   The reaction sequence experienced by migmatites may be an important factor in the preservation

538   of prograde suprasolidus monazite in peritectic minerals. For the modelled isobaric heating paths in

539   Figure 6, muscovite breakdown produces peritectic K-feldspar at ~700–750°C and the mode of K-

540   feldspar is expected to increase during biotite breakdown until ~810–850°C when biotite becomes

541   exhausted. For the 6 kbar isobaric heating path, cordierite grows at the expense of biotite. At

542   temperatures above biotite exhaustion, K-feldspar and cordierite are consumed. Therefore, any monazite

543   that may be generated at the margins of dissolving apatite over the interval 750–850°C has the potential

544   to be preserved in growing K-feldspar and/or cordierite, but at higher temperatures the rims of these

545   minerals may be resorbed, which may release some of the included monazite back into the melt. The

546   amount of apatite dissolution over this temperature range for a closed system is small and is predicted to

547   vary between 10% and 50% using the WL94 solubility equation for the modelled bulk P_2O_5

548   concentrations (Fig. 8). The amount is expected to be even less for the HW84 solubility equation and

549   much less for the modelled open-system scenarios (Fig. 8).

550   Garnet is an important peritectic mineral that is commonly targeted for *in situ* monazite U–Pb

551   geochronology (e.g. Korhonen et al., 2012; Yakymchuk et al., 2015). Similar to K-feldspar and

552   cordierite, garnet growth is predicted to occur at the expense of biotite and is consumed during heating

553   after biotite exhaustion in both closed- and open-system scenarios (Fig. 6). Therefore, garnet also has the

554   potential to capture monazite derived from apatite breakdown at T<810–850°C in the modelled

555   metapelite along the 6 kbar and 9 kbar isobaric heating paths (Fig. 6). Dumond et al. (2015) suggested

556   that some of their monazite inclusions in garnet are related to the breakdown of apatite (that now form

557   rounded inclusions in garnet) during heating and partial melting.

558   One mechanism that has been proposed to produce prograde suprasolidus monazite is Ostwald

559   ripening (e.g. Nemchin and Bodorkos, 2000). Ostwald ripening reduces the total surface free energy of a

560   system by preferentially dissolving smaller solids and precipitating this material on existing larger solids

561   (e.g. Tikare and Cawley, 1998). This is a possible mechanism for prograde monazite growth in

562   suprasolidus metamorphic rocks if there is no net decrease in the mode of monazite (e.g. Yakymchuk et

563   al., in press). However, monazite modes are expected to decrease during heating in both closed and open

564   systems to saturate the melt in the LREE. Therefore, for the scenarios modelled here, Ostwald ripening

565   may not be an appropriate mechanism for prograde monazite growth in an equilibrated system.

566

567   *6.4 Apatite dissolution and granite chemistry*

568   Apatite behaviour during partial melting has important implications for studies of the elemental

569   and isotopic variability of granites (e.g. Ayers and Harris, 1997; Zeng et al., 2005a, 2005b; Farina and

570 Stevens, 2011; Farina et al., 2014). Because apatite has a higher Sm/Nd ratio than monazite and the bulk

571 rock (e.g. Bea et al., 1994; Ayers and Harris, 1997), apatite will develop a relatively more radiogenic Nd

572 isotope value than the source. Detrital apatite also maintains its Nd isotope ratio during metamorphism

573 (e.g. Hammerli et al., 2014). Therefore, the dissolution of significant amounts of apatite (e.g. non-modal

574 melting) may result in a melt with a higher Nd isotope composition compared with the source (e.g. Zeng

575 et al., 2005a, 2005b).

576   The results of the modelling presented here indicate that the proportion of apatite dissolution is

577 sensitive to the bulk P_2O_5 concentration. For high P_2O_5 bulk concentrations, apatite progressively breaks

578 down towards higher T, but some apatite is expected to survive up to UHT conditions for both closed-

579 and open-system scenarios. Consequently, melt may develop a progressively more radiogenic Nd

580 isotope signature as melting proceeds. By contrast, if apatite is exhausted in a low P_2O_5 bulk

581 composition, the melt will become progressively less radiogenic due to the breakdown of minerals with

582 lower Sm/Nd ratios during further partial melting. However, monazite is expected to be the main

583 repository for Nd in pelites (e.g. Hammerli et al., 2014) and its breakdown will likely exert a first-order

584 control on the Nd isotope ratio of the melt.

585   The equilibrium modelling here predicts that melt remains saturated with phosphorus until

586 apatite is exhausted at high T. After the complete exhaustion of apatite during partial melting, additional

587 heating is predicted to generate melt that is undersaturated with respect to phosphorus. In addition to

588 apatite exhaustion, there are two important mechanisms that can produce undersaturated anatectic melt,

589 including: (1) inhibited accessory mineral dissolution due to kinetic factors (e.g. Harrison and Watson,

590 1984; Rapp and Watson, 1986) and (2) non-Henrian behaviour of trace elements during melt–solid

591 partitioning (Bea, 1996). Together, these mechanisms can result in a melt that is undersaturated in

592 phosphorus with respect to apatite, which may hinder prograde monazite growth above the solidus.

593   An additional factor that impacts apatite dissolution is the sequestration of grains included in

594 other minerals away from the reaction volume (e.g. Watson et al., 1989; Watt and Harley, 1993). In this

595   case, the effective bulk composition will be reduced and the high-temperature stability of the accessory

596   mineral will be lowered (e.g. Yakymchuk and Brown, 2014b). This has the potential to produce

597   undersaturated melt at temperatures below those predicted by using a measured P_2O_5 bulk concentration

598   and reduce the stability of apatite in the reacting volume of the rock (e.g. along grain boundaries). The

599   exhaustion of apatite also limits the use of apatite saturation temperatures to rocks where apatite was still

600   present at high temperature.

601

602   **7. Conclusions**

603   Apatite is predicted to progressively dissolve into anatectic melt during prograde suprasolidus

604   metamorphism in metapelites for both closed- and open-system scenarios. The stability of apatite is

605   primarily a function of melt composition, temperature and the bulk rock concentration of P_2O_5 and

606   whether melt loss is considered. For low bulk rock P_2O_5 concentrations, apatite may be completely

607   dissolved at UHT conditions whereas some apatite may survive at these conditions for high P_2O_5 bulk

608   rock concentrations. Melt loss generally extends the stability of apatite and monazite to higher

609   temperature. Partitioning of LREE into apatite reduces the high-temperature stability of monazite and

610   only minor prograde monazite growth may occur at the apatite–melt interface due to local oversaturation

611   of the melt in LREE. This monazite may be preserved as inclusions in peritectic minerals that shielded

612   them from further dissolution, but prograde suprasolidus monazite is less likely to survive in the matrix

613   of the rock.

614

619

References

Acosta-Vigil, A., London, D., Morgan, G.B., 2006. Experiments on the kinetics of partial melting of a leucogranite at 200 MPa H2O and 690–800 C: compositional variability of melts during the onset of H2O-saturated crustal anatexis. Contributions to Mineralogy and Petrology 151, 539-557.

Ague, J.J., 1991. Evidence for major mass transfer and volume strain during regional metamorphism of pelites. Geology 19, 855-858.

Ague, J.J., Eckert, J.O., 2012. Precipitation of rutile and ilmenite needles in garnet: Implications for extreme metamorphic conditions in the Acadian Orogen, U.S.A. American Mineralogist 97, 840-855.

Axler, J.A., Ague, J.J., 2015a. Oriented multiphase needles in garnet from ultrahigh-temperature granulites, Connecticut, U.S.A. American Mineralogist 100, 2254-2271.

Axler, J.A., Ague, J.J., 2015b. Exsolution of rutile or apatite precipitates surrounding ruptured inclusions in garnet from UHT and UHP rocks. Journal of Metamorphic Geology 33, 829-848.

Ayres, M., Harris, N., 1997. REE fractionation and Nd-isotope disequilibrium during crustal anatexis: constraints from Himalayan leucogranites. Chemical Geology 139, 249-269.

Bea, F., 1996a. Controls on the trace element composition of crustal melts. Geological Society of America Special Papers 315, 33-41.

Bea, F., 1996b. Residence of REE, Y, Th and U in granites and crustal protoliths; implications for the chemistry of crustal melts. Journal of Petrology 37, 521-552.

Bea, F., Fershtater, G., Corretgé, L.G., 1992. The geochemistry of phosphorus in granite rocks and the effect of aluminium. Lithos 29, 43-56.

Bea, F., Pereira, M.D., Stroh, A., 1994. Mineral/leucosome trace-element partitioning in a peraluminous migmatite (a laser ablation-ICP-MS study). Chemical Geology 117, 291-312.

Bingen, B., Demaiffe, D., Hertogen, J., 1996. Redistribution of rare earth elements, thorium, and uranium over accessory minerals in the course of amphibolite to granulite facies metamorphism: The role of apatite and monazite in orthogneisses from southwestern Norway. Geochimica et Cosmochimica Acta 60, 1341-1354.

Blereau, E., Clark, C., Taylor, R.J.M., Johnson, T.E., Fitzsimons, I.C.W., Santosh, M., 2016. Constraints on the timing and conditions of high-grade metamorphism, charnockite formation and fluid‑rock interaction in the Trivandrum Block, southern India. Journal of Metamorphic Geology 34, 527–549.

Brown, M., 2013. Granite: From genesis to emplacement. Geological Society of America Bulletin 125, 1079–1113.

Brown, C.R., Yakymchuk, C., Brown, M., Fanning, C.M., Korhonen, F.J., Piccoli, P.M., Siddoway, C.S., 2016. From Source to Sink: Petrogenesis of Cretaceous Anatectic Granites from the Fosdick Migmatite–Granite Complex, West Antarctica. Journal of Petrology 57, 1241-1278.

Catlos, E.J., 2013. Review: Versatile Monazite: resolving geological records and solving challenges in materials science. Generalizations about monazite: Implications for geochronologic studies. American Mineralogist 98, 819-832.

Clark, C., Fitzsimons, I.C.W., Healy, D., Harley, S.L., 2011. How does the continental crust get really hot? Elements 7, 235-240.

Clemens, J.D., 2006. Melting of the continental crust: fluid regimes, melting reactions, and source-rock fertility *In* Brown, M. and Rushmer, T. (eds), Evolution and Differentiation of the Continental Crust. Cambridge University Press.

Diener, J.F.A., Fagereng, Å., 2014. The influence of melting and melt drainage on crustal rheology during orogenesis. Journal of Geophysical Research: Solid Earth 119, 6193-6210.

Duc-Tin, Q., Keppler, H., 2015. Monazite and xenotime solubility in granitic melts and the origin of the lanthanide tetrad effect. Contributions to Mineralogy and Petrology 169, 1-26.

669 Dumond, G., Goncalves, P., Williams, M.L., Jercinovic, M.J., 2015. Monazite as a monitor of melting,
670   garnet growth and feldspar recrystallization in continental lower crust. Journal of Metamorphic
671   Geology 33, 735-762.
672 Farina, F., Dini, A., Rocchi, S., Stevens, G., 2014. Extreme mineral-scale Sr isotope heterogeneity in
673   granites by disequilibrium melting of the crust. Earth and Planetary Science Letters 399, 103-
674   115.
675 Farina, F., Stevens, G., 2011. Source controlled 87 Sr/86 Sr isotope variability in granitic magmas: the
676   inevitable consequence of mineral-scale isotopic disequilibrium in the protolith. Lithos 122, 189-
677   200.
678 Farley, K.A., Stockli, D.F., 2002. (U-Th)/He dating of phosphates: Apatite, monazite, and xenotime.
679   Reviews in Mineralogy and Geochemistry 48, 559-577.
680 Finger, F., Krenn, E., 2007. Three metamorphic monazite generations in a high-pressure rock from the
681   Bohemian Massif and the potentially important role of apatite in stimulating polyphase monazite
682   growth along a PT loop. Lithos 95, 103-115.
683 García-Arias, M., Corretgé, L.G., Castro, A., 2012. Trace element behavior during partial melting of
684   Iberian orthogneisses: An experimental study. Chemical Geology 292, 1-17.
685 Green, T.H., Watson, E.B., 1982. Crystallization of apatite in natural magmas under high pressure,
686   hydrous conditions, with particular reference to 'Orogenic' rock series. Contributions to
687   Mineralogy and Petrology 79, 96-105.
688 Guevara, V.E., Caddick, M.J., 2016. Shooting at a moving target: phase equilibria modelling of high-
689   temperature metamorphism. Journal of Metamorphic Geology 34, 209-235.
690 Hacker, B.R., Kylander-Clark, A.R.C., Holder, R., Andersen, T.B., Peterman, E.M., Walsh, E.O.,
691   Munnikhuis, J.K., 2015. Monazite response to ultrahigh-pressure subduction from U–Pb dating
692   by laser ablation split stream. Chemical Geology 409, 28-41.
693 Hammerli, J., Kemp, A.I.S., Spandler, C., 2014. Neodymium isotope equilibration during crustal
694   metamorphism revealed by in situ microanalysis of REE-rich accessory minerals. Earth and
695   Planetary Science Letters 392, 133-142.
696 Harley, S.L., 2016. A matter of time: The importance of the duration of UHT metamorphism. Journal of
697   Mineralogical and Petrological Sciences 111, 50-72.
698 Harlov, D.E., Marschall, H.R., Hanel, M., 2007. Fluorapatite-monazite relationships in granulite-facies
699   metapelites, Schwarzwald, southwest Germany. Mineralogical Magazine 71, 223-234.
700 Harrison, T.M., Watson, E.B., 1984. The behavior of apatite during crustal anatexis: equilibrium and
701   kinetic considerations. Geochimica et Cosmochimica Acta 48, 1467-1477.
702 Hermann, J., Rubatto, D., 2003. Relating zircon and monazite domains to garnet growth zones: age and
703   duration of granulite facies metamorphism in the Val Malenco lower crust. Journal of
704   Metamorphic Geology 21, 833-852.
705 Holland, T.J.B., Powell, R., 2011. An improved and extended internally consistent thermodynamic
706   dataset for phases of petrological interest, involving a new equation of state for solids. Journal of
707   Metamorphic Geology 29, 333-383.
708 Holness, M.B., Cesare, B., Sawyer, E.W., 2011. Melted rocks under the microscope: microstructures
709   and their interpretation. Elements 7, 247-252.
710 Johnson, T.E., Clark, C., Taylor, R.J.M., Santosh, M., Collins, A.S., 2015. Prograde and retrograde
711   growth of monazite in migmatites: An example from the Nagercoil Block, southern India.
712   Geoscience Frontiers 6, 373-387.
713 Kelsey, D.E., Clark, C., Hand, M., 2008. Thermobarometric modelling of zircon and monazite growth in
714   melt‐bearing systems: Examples using model metapelitic and metapsammitic granulites.
715   Journal of Metamorphic Geology 26, 199-212.

716 Kelsey, D.E., Hand, M., 2015. On ultrahigh temperature crustal metamorphism: phase equilibria, trace
717   element thermometry, bulk composition, heat sources, timescales and tectonic settings.
718   Geoscience Frontiers 6, 311-356.
719 Klimm, K., Blundy, J.D., Green, T.H., 2008. Trace Element Partitioning and Accessory Phase
720   Saturation during H_2O-Saturated Melting of Basalt with Implications for Subduction Zone
721   Chemical Fluxes. Journal of Petrology 49, 523-553.
722 Kohn, M.J., Malloy, M.A., 2004. Formation of monazite via prograde metamorphic reactions among
723   common silicates: implications for age determinations. Geochimica et Cosmochimica Acta 68,
724   101-113.
725 Korhonen, F.J., Brown, M., Grove, M., Siddoway, C.S., Baxter, E.F., Inglis, J.D., 2012. Separating
726   metamorphic events in the Fosdick migmatite–granite complex, West Antarctica. Journal of
727   Metamorphic Geology 30, 165-192.
728 Lederer, G.W., Cottle, J.M., Jessup, M.J., Langille, J.M., Ahmad, T., 2013. Timescales of partial melting
729   in the Himalayan middle crust: insight from the Leo Pargil dome, northwest India. Contributions
730   to Mineralogy and Petrology 166, 1415-1441.
731 London, D., Wolf, M.B., Morgan, G.B., Garrido, M.G., 1999. Experimental silicate–phosphate
732   equilibria in peraluminous granitic magmas, with a case study of the Alburquerque batholith at
733   Tres Arroyos, Badajoz, Spain. Journal of Petrology 40, 215-240.
734 Mayne, M.J., Moyen, J.F., Stevens, G., Kaislaniemi, L., 2016. Rcrust: a tool for calculating path-
735   dependent open system processes and application to melt loss. Journal of Metamorphic Geology
736   34, 663-682.
737 Montel, J.-M., 1986. Experimental determination of the solubility of Ce-monazite in SiO_2-Al_2O_3-K_2O-
738   Na_2O melts at 800 C, 2 kbar, under H_2O-saturated conditions. Geology 14, 659-662.
739 Montel, J.-M., 1993. A model for monazite/melt equilibrium and application to the generation of
740   granitic magmas. Chemical Geology 110, 127-146.
741 Nemchin, A.A., Bodorkos, S., 2000. Zr and LREE concentrations in anatectic melt as a function of
742   crystal size distributions of zircon and monazite in the source region. Geological Society of
743   America, Abstracts and Programs, Abstract 52286.
744 Parrish, R.R., 1990. U-Pb dating of monazite and its application to geological problems. Canadian
745   Journal of Earth Sciences 27, 1431-1450.
746 Piccoli, P.M., Candela, P.A., 2002. Apatite in igneous systems. Reviews in mineralogy and
747   geochemistry 48, 255-292.
748 Pichavant, M., Montel, J.-M., Richard, L.R., 1992. Apatite solubility in peraluminous liquids:
749   Experimental data and an extension of the Harrison-Watson model. Geochimica et
750   Cosmochimica Acta 56, 3855-3861.
751 Pyle, J.M., Spear, F.S., Wark, D.A., 2002. Electron Microprobe Analysis of REE in Apatite, Monazite
752   and Xenotime: Protocols and Pitfalls. Reviews in mineralogy and geochemistry 48, 337-362.
753 Powell, R., Holland, T.J.B., 1988. An internally consistent dataset with uncertainties and correlations: 3.
754   Applications to geobarometry, worked examples and a computer program. Journal of
755   Metamorphic Geology 6, 173-204.
756 Prowatke, S., Klemme, S., 2006. Trace element partitioning between apatite and silicate melts.
757   Geochimica et Cosmochimica Acta 70, 4513-4527.
758 Rakovan, J., Reeder, R.J., 1996. Intracrystalline rare earth element distributions in apatite: Surface
759   structural influences on incorporation during growth. Geochimica et Cosmochimica Acta 60,
760   4435-4445.
761 Rapp, R.P., Ryerson, F.J., Miller, C.F., 1987. Experimental evidence bearing on the stability of monazite
762   during crustal anaatexis. Geophysical Research Letters 14, 307-310.

Rapp, R.P., Watson, E.B., 1986. Monazite solubility and dissolution kinetics: implications for the thorium and light rare earth chemistry of felsic magmas. Contributions to Mineralogy and Petrology 94, 304-316.

Rocha, B.C., Moraes, R., Möller, A., Cioffi, C.R., Jercinovic, M.J., 2016. Timing of anatexis and melt crystallization in the Socorro–Guaxupé Nappe, SE Brazil: Insights from trace element composition of zircon, monazite and garnet coupled to U Pb geochronology. Lithos. Doi: 10.1016/j.lithos.2016.05.020.

Rosenberg, C.L., Handy, M.R., 2005. Experimental deformation of partially melted granite revisited: implications for the continental crust. Journal of Metamorphic Geology 23, 19-28.

Sawyer, E.W., 1991. Disequilibrium melting and the rate of melt–residuum separation during migmatization of mafic rocks from the Grenville Front, Quebec. Journal of Petrology 32, 701-738.

Sawyer, E.W., 1999. Criteria for the recognition of partial melting. Physics and Chemistry of the Earth, Part A: Solid Earth and Geodesy 24, 269-279.

Sawyer, E.W., 2014. The inception and growth of leucosomes: microstructure at the start of melt segregation in migmatites. Journal of Metamorphic Geology 32, 695-712.

Smith, M.P., Yardley, B.W.D. 1999. Fluid evolution during metamorphism of the Otago Schist, New Zealand: (II) Influence of detrital apatite on fluid salinity. Journal of Metamorphic Geology 17, 187-193.

Spear, F.S., Pyle, J.M., 2002. Apatite, monazite, and xenotime in metamorphic rocks. Reviews in mineralogy and geochemistry 48, 293-335.

Spear, F.S., Pyle, J.M., 2010. Theoretical modeling of monazite growth in a low-Ca metapelite. Chemical Geology 273, 111-119.

Spear, F.S., Kohn, M.J., Cheney, J.T., 1999. P-T paths from anatectic pelites. Contributions to Mineralogy and Petrology 134, 17-32.

Stepanov, A.S., Hermann, J., Rubatto, D., Rapp, R.P., 2012. Experimental study of monazite/melt partitioning with implications for the REE, Th and U geochemistry of crustal rocks. Chemical Geology 300, 200-220.

Taylor, R.J.M., Kirkland, C.L., Clark, C., 2016. Accessories after the facts: Constraining the timing, duration and conditions of high-temperature metamorphic processes. Lithos.

Taylor, S.R., McLennan, S.M., 1985. The Continental Crust: Its composition and evolution. Blackwell Scientific, Oxford.

Tikare, V., Cawley, J.D., 1998. Application of the Potts model to simulation of Ostwald ripening. Journal of the American Ceramic Society 81, 485-491.

Toplis, M.J., Dingwell, D.B., 1996. The variable influence of P_2O_5 on the viscosity of melts of differing alkali/aluminium ratio: Implications for the structural role of phosphorus in silicate melts. Geochimica et Cosmochimica Acta 60, 4107-4121.

Vigneresse, J.L., Burg, J.P., 2000. Continuous vs. discontinuous melt segregation in migmatites: insights from a cellular automaton model. Terra Nova 12, 188-192.

Villaseca, C., Martín Romera, C., De la Rosa, J., Barbero, L., 2003. Residence and redistribution of REE, Y, Zr, Th and U during granulite-facies metamorphism: behaviour of accessory and major phases in peraluminous granulites of central Spain. Chemical Geology 200, 293-323.

Watson, E.B., 1979. Apatite saturation in basic to intermediate magmas. Geophysical Research Letters 6, 937-940.

Watson, E.B., Green, T.H., 1981. Apatite/liquid partition coefficients for the rare earth elements and strontium. Earth and Planetary Science Letters 56, 405-421.

Watson, E.B., Harrison, T.M., 1983. Zircon saturation revisited: temperature and composition effects in a variety of crustal magma types. Earth and Planetary Science Letters 64, 295-304.

811 Watson, E.B., Vicenzi, E.P., Rapp, R.P., 1989. Inclusion/host relations involving accessory minerals in
812   high-grade metamorphic and anatectic rocks. Contributions to Mineralogy and Petrology 101,
813   220-231.
814 Watt, G.R., Harley, S.L., 1993. Accessory phase controls on the geochemistry of crustal melts and
815   restites produced during water-undersaturated partial melting. Contributions to Mineralogy and
816   Petrology 114, 550-566.
817 Webster, J.D., Piccoli, P.M., 2015. Magmatic apatite: a powerful, yet deceptive, mineral. Elements 11,
818   177-182.
819 White, R.W., Pomroy, N.E., Powell, R., 2005. An in situ metatexite–diatexite transition in upper
820   amphibolite facies rocks from Broken Hill, Australia. Journal of Metamorphic Geology 23, 579-
821   602.
822 White, R.W., Powell, R., 2002. Melt loss and the preservation of granulite facies mineral assemblages.
823   Journal of Metamorphic Geology 20, 621-632.
824 White, R.W., Powell, R., Holland, T.J.B., Johnson, T.E., Green, E.C.R., 2014a. New mineral activity–
825   composition relations for thermodynamic calculations in metapelitic systems. Journal of
826   Metamorphic Geology 32, 261-286.
827 White, R.W., Powell, R., Johnson, T.E., 2014b. The effect of Mn on mineral stability in metapelites
828   revisited: new a‑x relations for manganese‑bearing minerals. Journal of Metamorphic Geology
829   32, 809-828.
830 Wolf, M.B., London, D., 1994. Apatite dissolution into peraluminous haplogranitic melts: an
831   experimental study of solubilities and mechanisms. Geochimica et Cosmochimica Acta 58,
832   4127-4145.
833 Wolf, M.B., London, D., 1995. Incongruent dissolution of REE-and Sr-rich apatite in peraluminous
834   granitic liquids: Differential apatite, monazite, and xenotime solubilities during anatexis.
835   American Mineralogist 80, 765-775.
836 Yakymchuk, C., Brown, M., 2014a. Consequences of open-system melting in tectonics. Journal of the
837   Geological Society 171, 21-40.
838 Yakymchuk, C., Brown, M., 2014b. Behaviour of zircon and monazite during crustal melting. Journal of
839   the Geological Society 171, 465–479.
840 Yakymchuk, C., Brown, M., Clark, C., Korhonen, F.J., Piccoli, P.M., Siddoway, C.S., Taylor, R.J.M.,
841   Vervoort, J.D., 2015. Decoding polyphase migmatites using geochronology and phase equilibria
842   modelling. Journal of Metamorphic Geology 33, 203-230.
843 Yakymchuk, C., Clark, C., White, R.W., *in press*. Phase Relations, Reaction Sequences and
844   Petrochronology in: Kohn, M.J., Lanari, P. (Eds.), Petrochronology, doi: 10.2138/rmg.2017.83.2.
845 Yang, P., Rivers, T., The origin of Mn and Y annuli in garnet and the thermal dependence of P in garnet
846   and Y in apatite in calc-pelite and pelite, Gagnon terrane, western Labrador. Geological
847   Materials Research 4, 35p.
848 Zeng, L., Asimow, P.D., Saleeby, J.B., 2005a. Coupling of anatectic reactions and dissolution of
849   accessory phases and the Sr and Nd isotope systematics of anatectic melts from a
850   metasedimentary source. Geochimica et Cosmochimica Acta 69, 3671-3682.
851 Zeng, L., Saleeby, J.B., Asimow, P., 2005b. Nd isotope disequilibrium during crustal anatexis: A record
852   from the Goat Ranch migmatite complex, southern Sierra Nevada batholith, California. Geology
853   33, 53-56.
854

855 **Figure captions**

856   **Figure 1.** *P–T* pseudosection for an average amphibolite-facies metapelite (modified from Yakymchuk

857   et al., *in press*). The dashed line is the solidus. The two isobaric heating paths are used to evaluate

858   closed-system versus open-system behaviour in Figures 6–9.

859

860   **Figure 2.** Contours for the proportion and composition of anatectic melt important for the modelling the

861   behaviour of apatite and monazite. (a) The proportion of anatectic melt in mol.% (approximately

862   equivalent to vol.%) in the metapelite in a closed system. (b) The aluminum saturation value of melt. (c)

863   the weight percentage of SiO_2 in melt. (d) the weight percentage of H_2O in melt. The dashed line is the

864   solidus.

865

866   **Figure 3.** Contours for saturation concentrations of melt in P_2O_5 (wt.%) using the apatite solubility

867   equations of (a) Harrison and Watson (1984): HW84, and (b) Wolf and London (1994): WL94. (c)

868   Contours for saturation concentrations of melt in LREE (ppm) using the solubility equation of Stepanov

869   et al. (2012) for monazite. The dashed line is the solidus.

870

871   **Figure 4.** Contours for the amount of apatite dissolution (%) in a closed system using the apatite

872   solubility equations of Harrison and Watson (1984): HW84, and Wolf and London (1994): WL94. The

873   assumed bulk rock concentration of LREE is 150 ppm and various concentrations of P_2O_5 are indicated.

874   The dashed line is the solidus.

875

876   **Figure 5.** Contours for the amount of monazite dissolution in a closed system comparing the difference

877   between excluding apatite from the system (e.g. Kelsey et al., 2008; Yakymchuk and Brown, 2014) and

878   including it. (a) Monazite dissolution contours (%) for the apatite-free scenario. (b) Monazite dissolution

879   contours (%) that include apatite using the Harrison and Watson (1984) apatite solubility equation. (c)

880   Monazite dissolution contours (%) that include apatite using the Wolf and London (1994) apatite

881   solubility equation. The dashed line is the solidus.

882

883   **Figure 6.** Mode–temperature diagrams illustrating the changes in modal proportions (mol.%

884   approximately equivalent to vol.%) along two isobaric heating paths from 650 to 950°C at 9 kbar (a,b)

885   and 6 kbar (c, d) for closed- and open-system scenarios. (e–h) The concentration of P_2O_5 (wt.%) in the

886   system during open- and closed-system scenarios for the two modelled isobaric heating paths. (i–j) The

887   concentration of LREE (ppm) in the system during open and closed-system scenarios for the two

888   modelled isobaric heating paths. WL94: apatite solubility equation of Wolf and London (1994). HW84:

889   apatite solubility equation of Harrison and Watson (1994). Melt loss (ML) events are indicated by the

890   vertical lines for the open-system scenarios.

891

892   **Figure 7.** Concentration of LREE and P_2O_5 in melt for the two isobaric heating paths in Fig. 1 using the

893   Wolf and London (1994) apatite solubility equation. Results for initial bulk P_2O_5 contents of 0.1, 0.3 and

894   0.5 wt.% for the open-system scenarios are shown. The concentrations of LREE and P_2O_5 in melt are

895   buffered to the saturation values when monazite and apatite are present. After apatite or monazite

896   exhaustion, the concentrations of LREE and P_2O_5 in melt are diluted during further partial melting.

897

898   **Figure 8.** (a–d) Amounts of apatite dissolution required to maintain phosphorus saturation of the melt

899   for closed- and open-system scenarios along two isobaric heating paths. In all cases, open-system

900   behaviour extends the stability of apatite to higher temperatures compared to the closed system. (e–h)

901   Amounts of monazite dissolution required to maintain LREE saturation of the melt for closed and open

902   system scenarios along two isobaric heating paths. In all cases, open-system behaviour extends the

903   stability of monazite to higher temperatures compared to the closed system. WL94: apatite solubility

904 equation of Wolf and London (1994). HW84: apatite solubility equation of Harrison and Watson (1994).

905 Melt loss (ML) events are indicated by the vertical lines.

906

907 **Figure 9.** Amount of monazite remaining relative to the amount present at the solidus for various molar

908 ratios of the LREE to the sum of all cations in monazite (X_{mnz}^{LREE}) for the open-system isobaric heating

909 paths at 9 kbar (a) and 6 kbar (b). The apatite solubility equation is from Wolf and London (1994). The

910 starting bulk concentration of P_2O_5 is 0.3 wt.%.

911

912 **Figure 10.** The relationship between temperature, time, grain size and the H_2O content of the melt for

913 apatite and monazite dissolution. (a) Apatite dissolution (modified from Rapp and Watson, 1986). (b)

914 Monazite dissolution (modified from Harrison and Watson, 1984).

915 **Table 1.** Bulk composition used in phase equilibria modelling (mol.%).

Figures	ML	H$_2$O	SiO$_2$	Al$_2$O$_3$	CaO	MgO	FeO	K$_2$O	Na$_2$O	TiO$_2$	MnO	O
Closed system – solidus saturated with H$_2$O at 9 kbar												
1–6, 8		6.24	60.55	12.80	1.49	5.18	7.52	2.76	1.88	0.85	0.16	0.60
Open system – Isobaric Heating at 9 kbar												
	solidus	6.24	60.55	12.80	1.49	5.18	7.52	2.76	1.88	0.85	0.16	0.60
6–9	ML1	4.93	60.67	13.13	1.55	5.50	7.98	2.76	1.77	0.90	0.17	0.64
6–9	ML2	3.56	60.80	13.48	1.61	5.84	8.47	2.75	1.67	0.96	0.19	0.68
6–9	ML3	2.32	60.78	13.83	1.67	6.20	8.98	2.73	1.56	1.02	0.20	0.72
6–9	ML4	1.17	60.64	14.17	1.72	6.57	9.52	2.70	1.46	1.08	0.21	0.77
6–9	ML5	0.18	60.33	14.50	1.76	6.96	10.08	2.64	1.37	1.15	0.22	0.82
Open system – Isobaric Heating at 6 kbar												
6–9	solidus	5.15	61.23	12.94	1.50	5.24	7.61	2.79	1.90	0.86	0.17	0.61
6–9	ML1	4.10	61.10	13.27	1.57	5.56	8.07	2.77	1.82	0.91	0.18	0.65
6–9	ML2	3.16	60.84	13.60	1.64	5.90	8.55	2.74	1.73	0.97	0.19	0.69
6–9	ML3	2.27	60.48	13.93	1.71	6.25	9.05	2.69	1.65	1.03	0.20	0.73
6–9	ML4	1.40	60.05	14.27	1.78	6.63	9.59	2.62	1.59	1.10	0.21	0.78
6–9	ML5	0.81	59.36	14.58	1.84	7.01	10.13	2.53	1.53	1.16	0.23	0.83
6–9	ML6	0.38	58.51	14.88	1.89	7.41	10.69	2.41	1.49	1.24	0.24	0.88

916 *ML: melt loss event*

Figure 1

+ liq + ilm
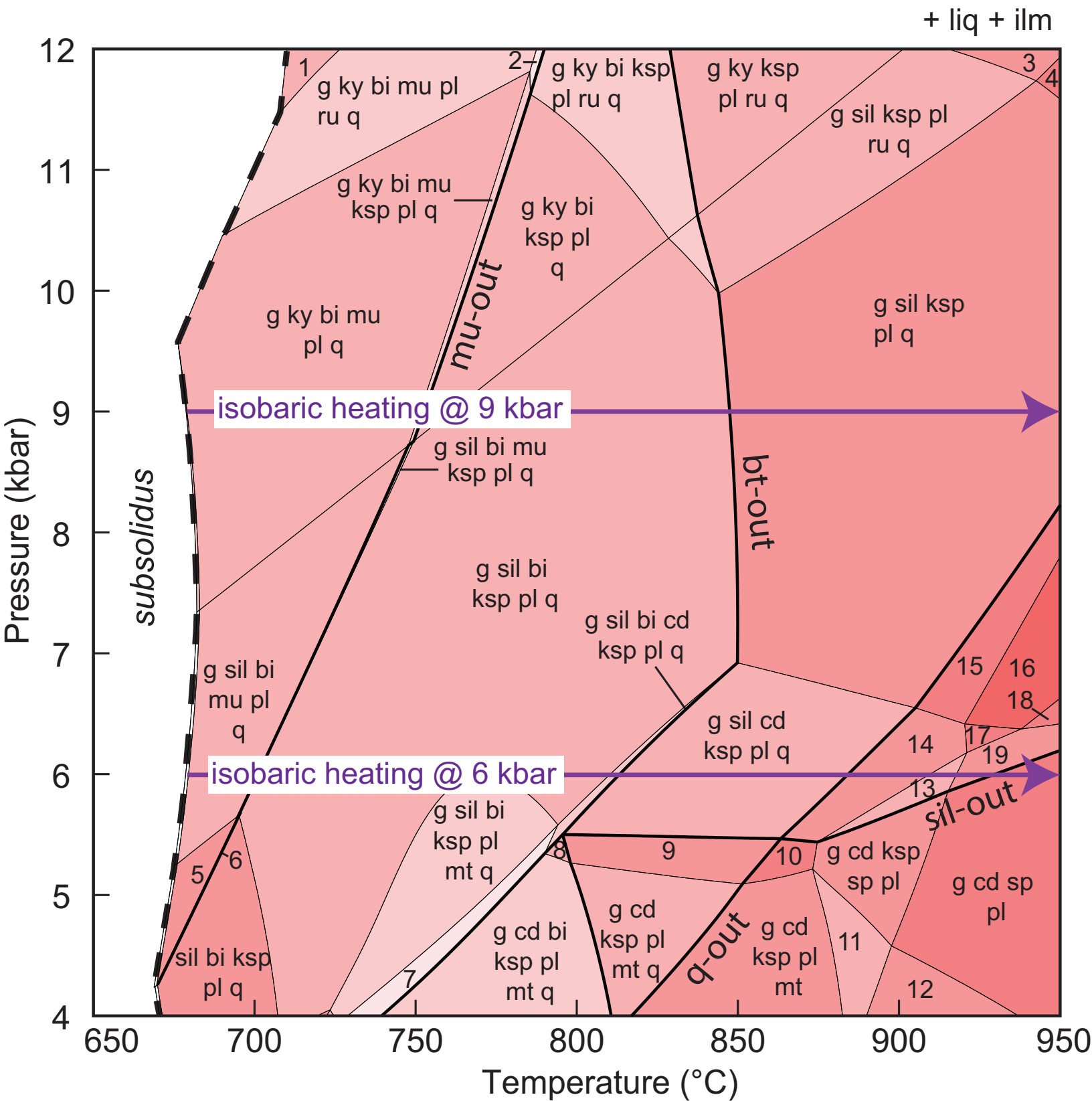
1: g bi mu pl ru q
2: g ky bi mu ksp pl ru q
3: g sil ksp ru q
4: g sil ksp q
5: sil bi mu pl q
6: sil ksp bi mu pl q
7: g sil cd bi ksp pl mt q

8: g cd bi ksp pl q
9: g cd ksp pl q
10: g cd ksp pl
11: g cd ksp sp pl mt
12: g cd sp pl mt
13: g sil cd ksp sp pl
14: g sil cd ksp pl

15: g sil ksp pl
16: g sil pl
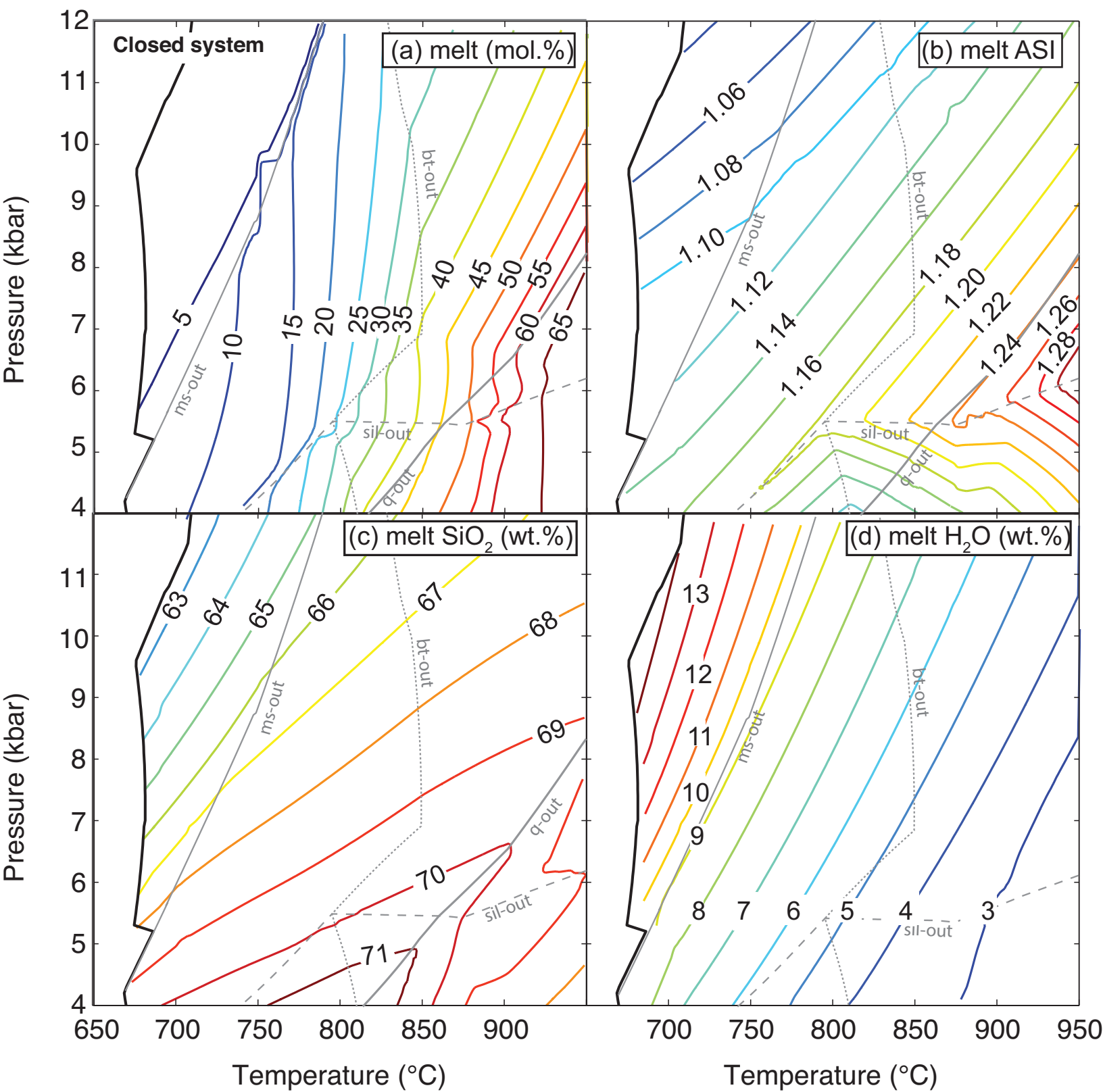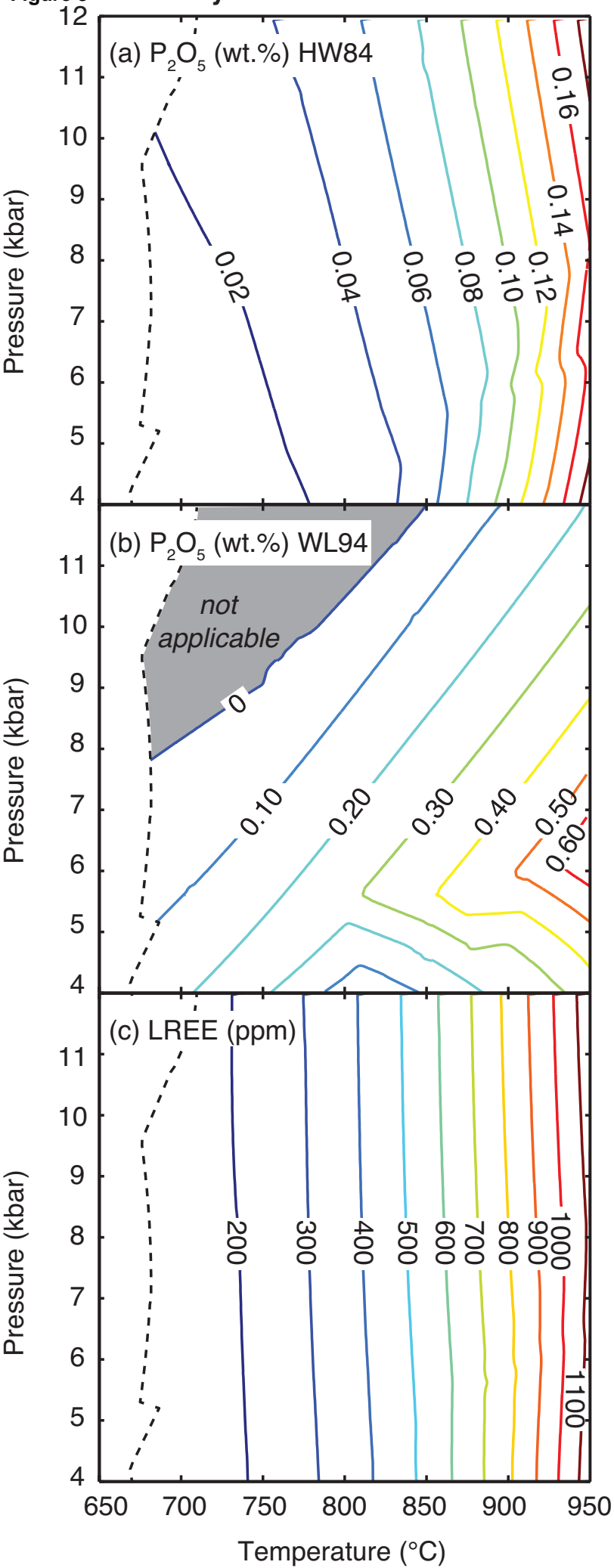17: g sil cd pl
18: g sil sp pl
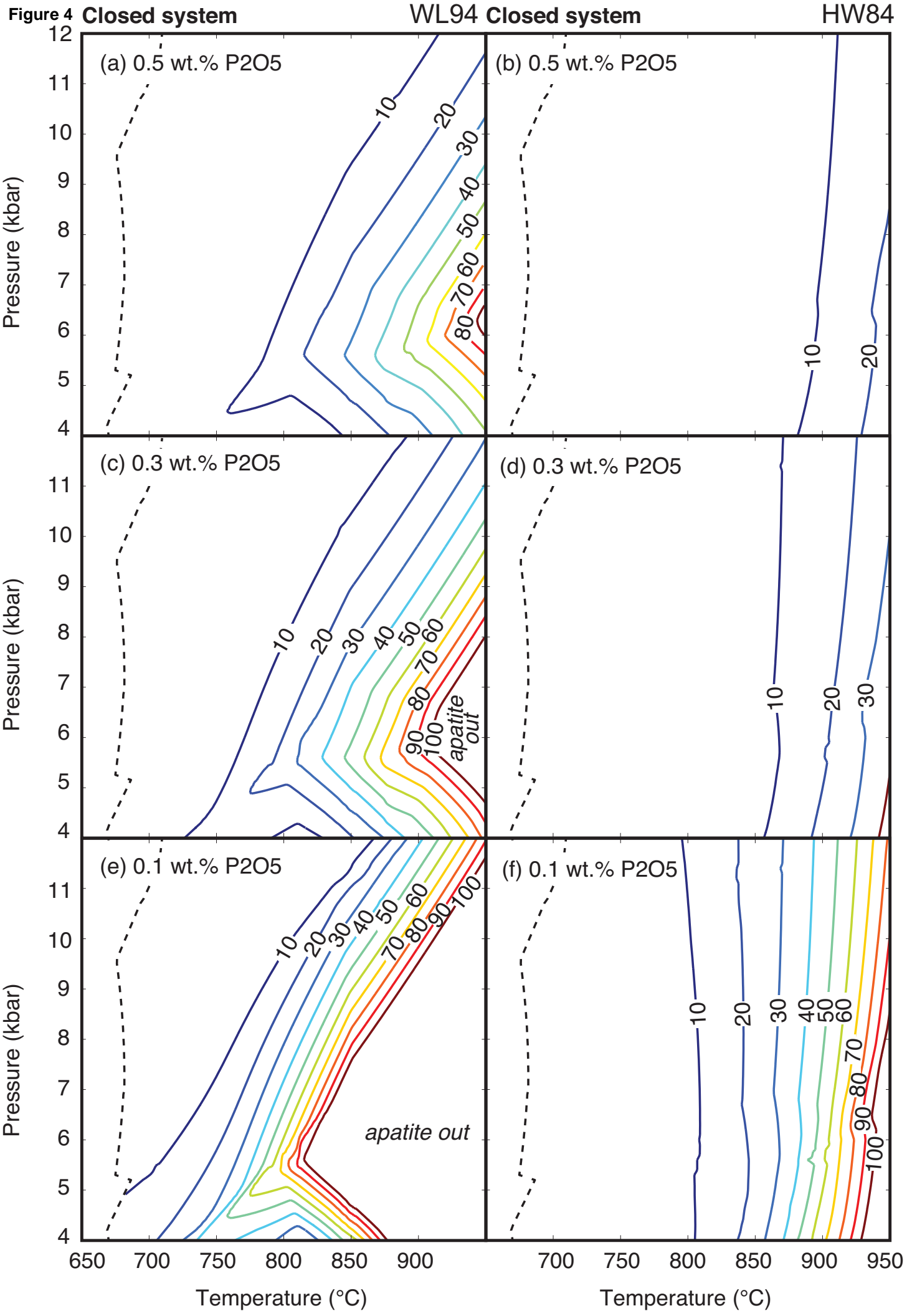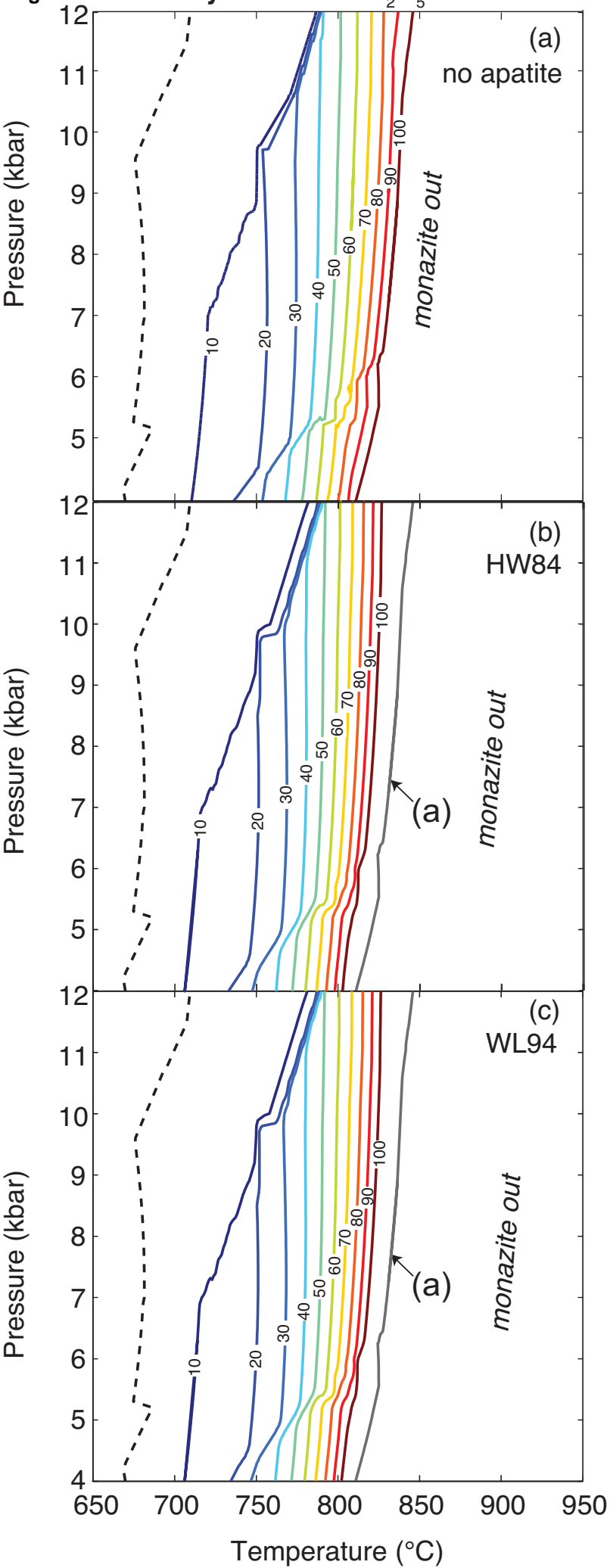19: g sil cd sp pl

Figure 2

Figure 3 **Closed system**

(a) P_2O_5 (wt.%) HW84

(b) P_2O_5 (wt.%) WL94

not applicable

(c) LREE (ppm)

Figure 4

Figure 5 **Closed system** $P_2O_5 = 0.30$ wt.%

(a) no apatite

monazite out

(b) HW84

monazite out

(a)

(c) WL94

monazite out

(a)

Pressure (kbar)

Temperature (°C)

Figure 6

Isobaric heating at 9 kbar

Isobaric heating at 6 kbar

Figure 7

Figure 8

Isobaric heating at 9 kbar

Isobaric heating at 6 kbar
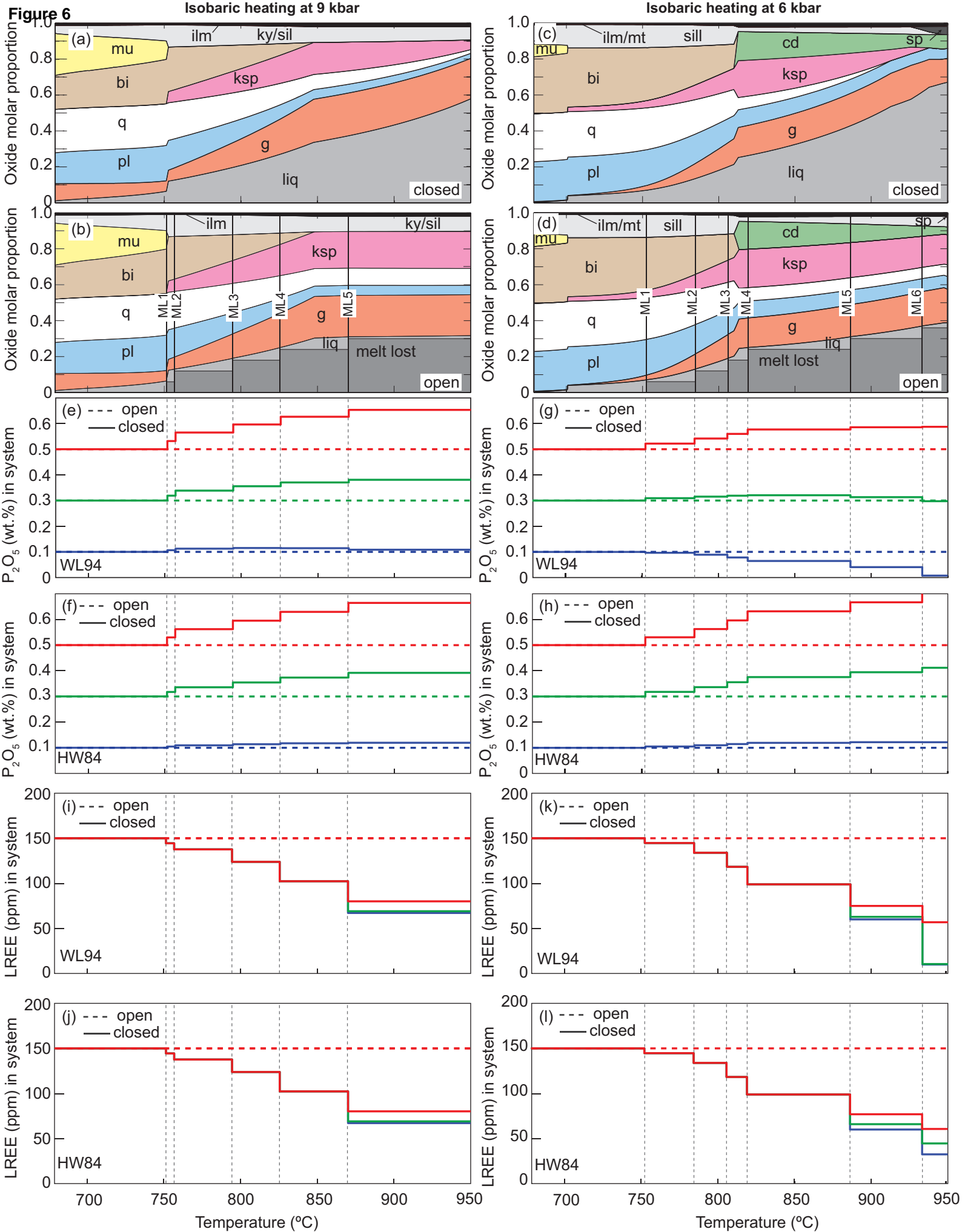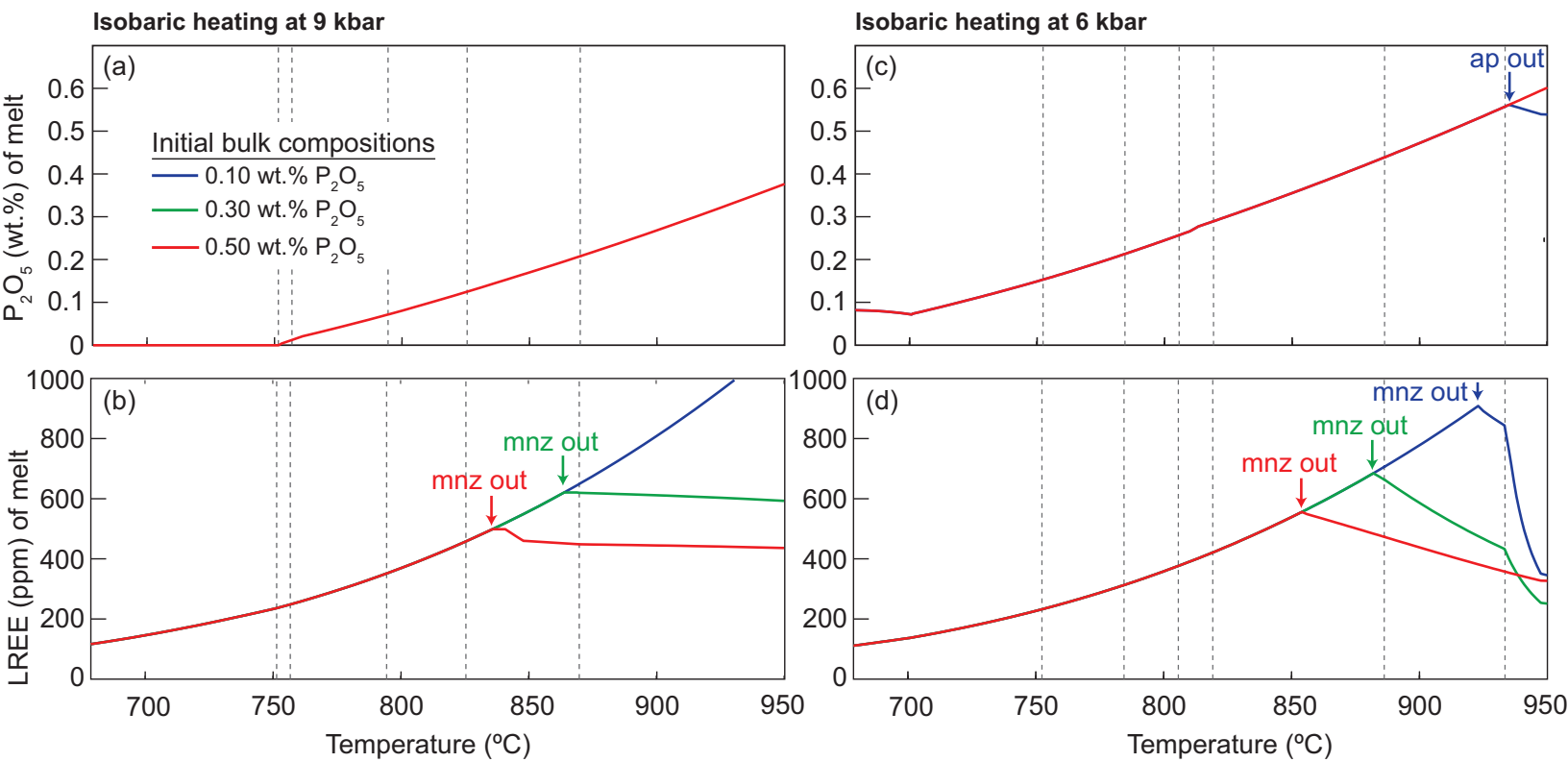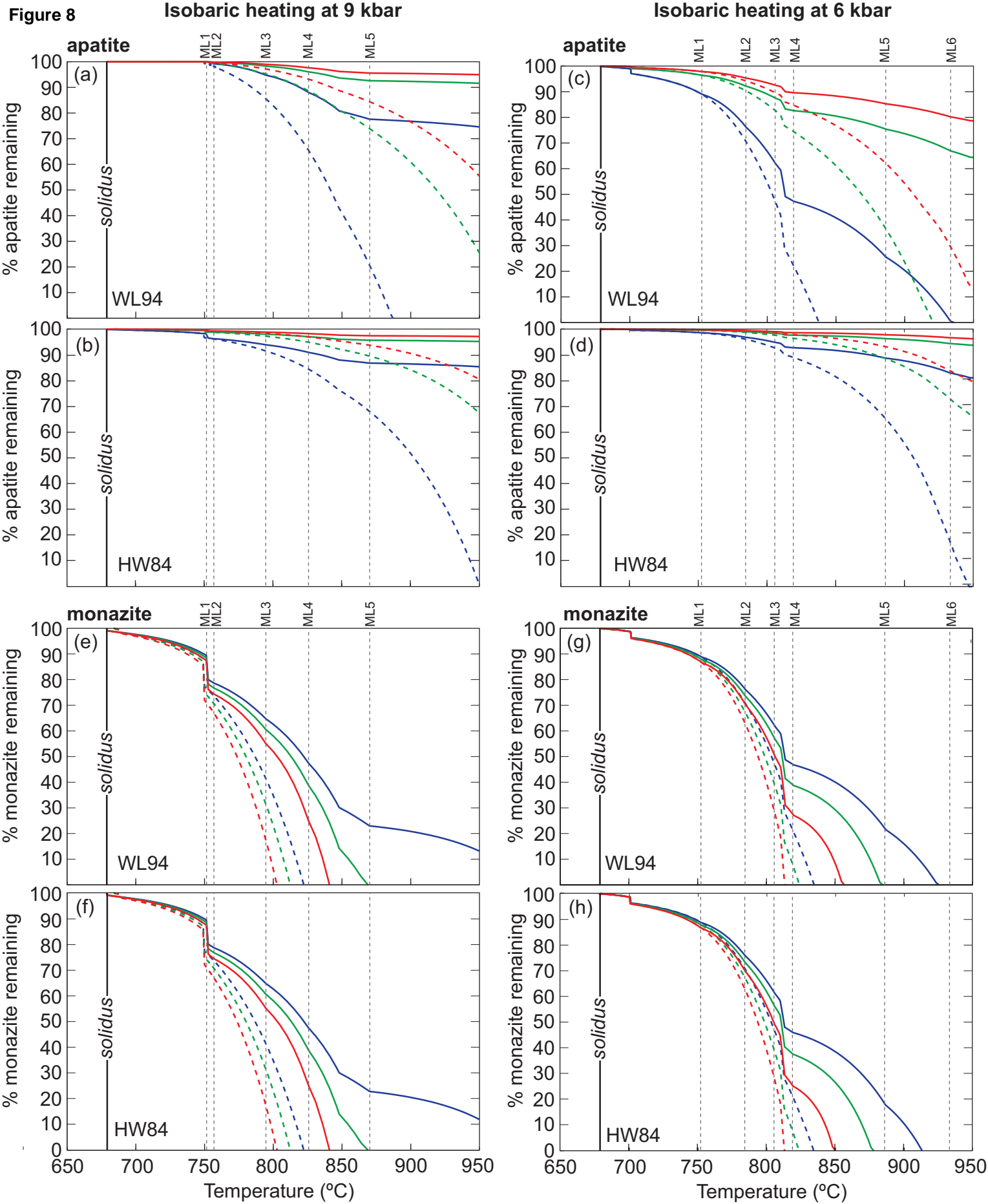
Closed system
- - - - 0.10 wt.% P₂O₅
- - - - 0.30 wt.% P₂O₅
- - - - 0.50 wt.% P₂O₅

Open system
—— 0.10 wt.% P₂O₅
—— 0.30 wt.% P₂O₅
—— 0.50 wt.% P₂O₅

Figure 9
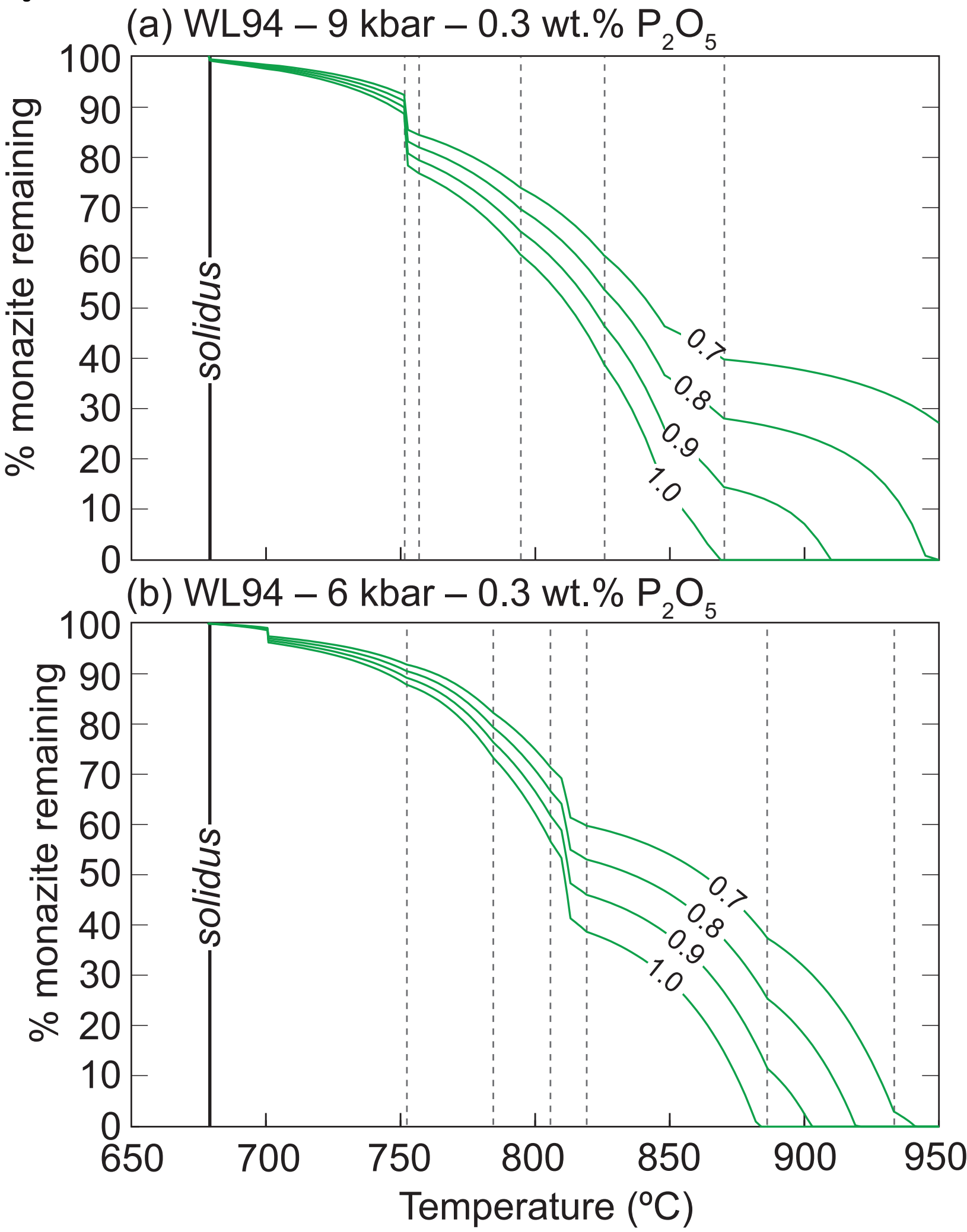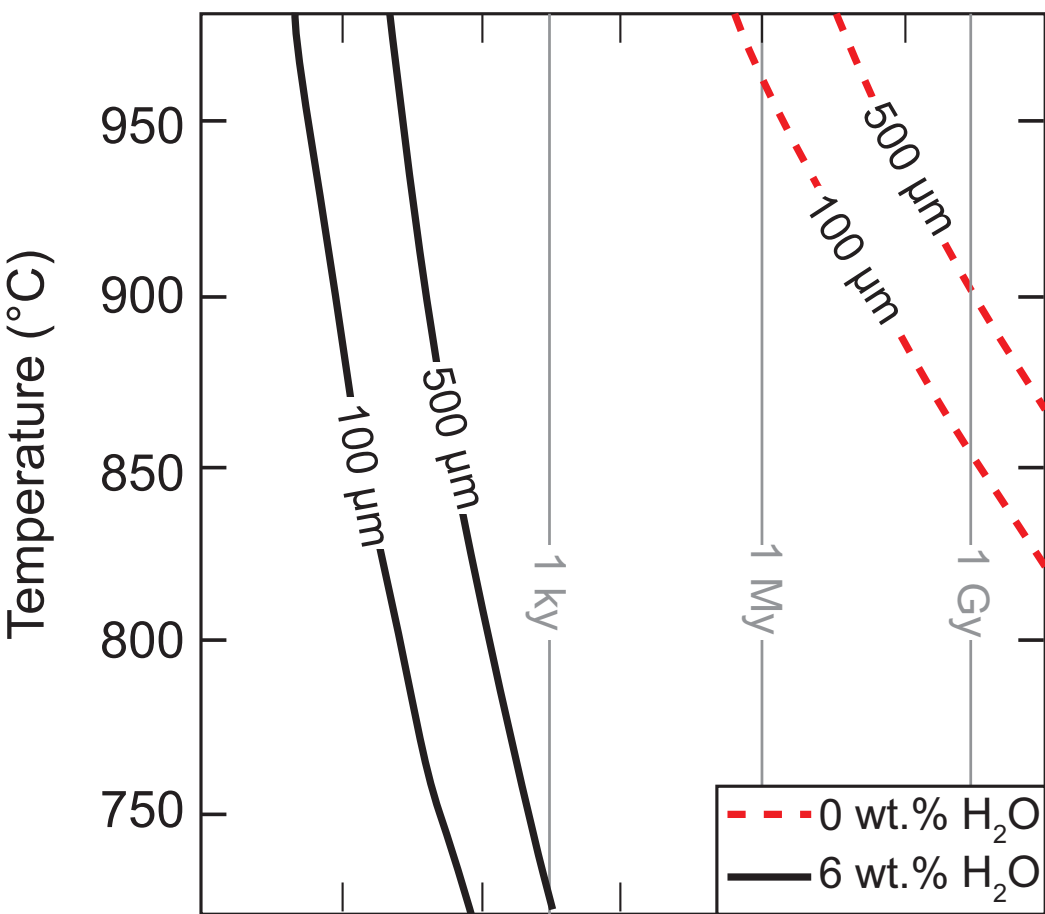

(a) WL94 – 9 kbar – 0.3 wt.% P_2O_5

(b) WL94 – 6 kbar – 0.3 wt.% P_2O_5

Figure 10

(a) apatite

(b) monazite